Nanoscale Advances

ROYAL SOCIETY OF CHEMISTRY

PAPER

View Article Online
View Journal | View Issue

Cite this: *Nanoscale Adv.*, 2023, **5**, 1433

Synthesis of a crystalline zeolitic imidazole framework-8 nano-coating on single environment-sensitive viral particles for enhanced immune responses†

Liuyang Wang,‡[ab] Xuan Lin,‡[b] Yanan Sheng,[b] Hongyu Zhu,[bc] Zhengjun Li,[b] Zhiguo Su,[b] Rong Yu*[a] and Songping Zhang *[b]

Encapsulating antigens with zeolitic imidazole framework-8 (ZIF-8) exhibits many advantages in vaccine development. However, most viral antigens with complex particulate structures are sensitive to pH or ionic strength, which cannot tolerate harsh synthesis conditions of ZIF-8. Balancing the viral integrity and the growth of ZIF-8 crystals is crucial for the successful encapsulation of these environment-sensitive antigens in ZIF-8. Here, we explored the synthesis of ZIF-8 on inactivated foot and mouth disease virus (known as 146S), which is easily disassociated into no immunogenic subunits under the existing ZIF-8 synthesis conditions. Our results showed that intact 146S could be encapsulated into ZIF-8 with high embedding efficiency by lowering the pH of the 2-MIM solution to 9.0. The size and morphology of 146S@ZIF-8 could be further optimized by increasing the amount of Zn^{2+} or adding cetyltrimethylammonium bromide (CTAB). 146S@ZIF-8 with a uniform diameter of about 49 nm could be synthesized by adding 0.01% CTAB, which was speculated to be composed of single 146S armored with nanometer-scale ZIF-8 crystal networks. Plenty of histidine on the 146S surface forms a unique His-Zn-MIM coordination in the near vicinity of 146S particles, which greatly increases the thermostability of 146S by about 5 °C, and the nano-scale ZIF-8 crystal coating exhibited extraordinary stability to resist EDTE-treatment. More importantly, the well-controlled size and morphology enabled 146S@ZIF-8(0.01% CTAB) to facilitate antigen uptake. The immunization of 146S@ZIF-8(4×Zn^{2+}) or 146S@ZIF-8(0.01% CTAB) significantly enhanced the specific antibody titers and promoted the differentiation of memory T cells without adding another immunopotentiator. This study reported for the first time the strategy of the synthesis of crystalline ZIF-8 on an environment-sensitive antigen and demonstrated that the nano-size and appropriate morphology of ZIF-8 are crucial to exert adjuvant effects, thus expanding the application of MOFs in vaccine delivery.

Received 1st November 2022
Accepted 6th February 2023

DOI: 10.1039/d2na00767c

rsc.li/nanoscale-advances

Introduction

Metal–organic frameworks (MOFs) are a class of coordination polymers, consisting of metal ions or clusters linked together by chemically mutable organic groups.[1] The porous property, high loading capacity, structural stability, fine-turned pore size/shape, and functionality make MOFs an emerging platform material for drug delivery.[2–4] Among them, zeolitic imidazole framework-8 (ZIF-8), which is synthesized from 2-methyl-imidazole (2-MIM) and Zn^{2+}, is the most attractive one for biomacromolecule drugs, due to its excellent biocompatibility, environmentally sensitive degradation properties, and facile synthesis in the aqueous phase.[5–9] Since the first report on the construction of MOF-based vaccine synthesized by biomimetic mineralized growth of ZIF-8 onto the surface of ovalbumin (OVA) and attaching the cytosine–phosphate–guanine

[a]*Key Laboratory of Drug-Targeting and Drug Delivery System of the Ministry of Education, West China School of Pharmacy, Sichuan University, Chengdu, 610041, China. E-mail: yurong@scu.edu.cn*

[b]*State Key Laboratory of Biochemical Engineering, Institute of Process Engineering, Chinese Academy of Sciences, Beijing 100190, China. E-mail: spzhang@ipe.ac.cn; Tel: +86-10-82544958*

[c]*Division of Molecular Science, Graduate School of Science and Technology, Gunma University, Kiryu, 376-8515, Japan*

† Electronic supplementary information (ESI) available: HPSEC analysis of 146S@ZIF-8 lysates, energy discrete spectroscopy (EDS) images of selected samples, the reaction speed of 146S@ZIF-8(1×Zn^{2+}), PXRD images of ZIF-8 synthesized under different conditions, thermal stability analysis of optimized samples, typical strategies for dividing gate in flow cytometry, detection of specific antibody subtypes in serum of mice after immunization, and comparison of biochemical indices of mice after immunization. The underlying raw images of electrophoretic gel. See DOI: https://doi.org/10.1039/d2na00767c

‡ These authors contributed equally to this work.

oligodeoxynucleotides (CpG ODNs) in/on ZIF-8, the exploration of ZIF-8 in the delivery of vaccine antigens has been attracting more attention.[10–15] Research efforts have demonstrated that in addition to the typical advantages of ZIF-8 in drug delivery, the MOF-based vaccine platform also exhibited adjuvant effects by stabilizing antigens,[11] promoting antigen presentation,[10] co-delivering other adjuvants[14,16] and inducing multiple immune responses.[15]

Encouraged by the successes in the synthesis and delivery of OVA@ZIF-8 vaccine, researchers started trying to synthesize viral vaccines by encapsulating various types of viral antigens, including virus-like particles, live viruses, and viral vectors into ZIF-8. It was discovered that, however, unlike the model antigen OVA having a simple and stable structure that can tolerate relatively harsh conditions during the synthesis of ZIF-8, the encapsulation of these proteinaceous particles with complex structures into MOF materials faces many challenges. Firstly, most viral antigens are sensitive to environments, such as pH and ionic strength.[17–19] Unfortunately, during the synthesis of ZIF-8, strong alkaline conditions (approx. pH 11.0) are essential to deprotonate the *N*-pyrrole atom in the 2-MIM ligand. These harsh conditions may lead to the deactivation or even destruction of the viral antigens. Secondly, the potency of the vaccine is highly dependent on the size, morphology, and surface properties of the adjuvant materials.[20] When the viral antigen with a complex particulate structure is encapsulated with ZIF-8, the morphological regulation on their surface becomes more complicated,[13] as the local curvature of the viral particles acting as the parent core may impose some subtle but profound effect on the crystal growth.[21] For instance, the biomineralization of ZIF-8 on Tobacco mosaic virus (TMV), a rod-shaped virus, generated a highly anisotropic rod shape crystal structure grown according to the TMV structure.[22] While for small isotropic materials, such as the polio virus about 30 nm in diameter, high stress–strain would be induced by the MOF shell growth on it. As a consequence, the synthetic methods will possibly encapsulate multiple viral nanoparticles into a larger crystal, making injection administration and *in vivo* endocytosis by cells difficult.[23]

In order to address these difficulties, the synthetic conditions usually have to be adjusted, thus deviating from the optimal conditions for crystalline formation of ZIF-8. For instance, when live Newcastle disease virus (NDV) was encapsulated in crystalline ZIF-8, the viral titer decreased significantly; therefore, only amorphous ZIF-8 coordination polymer could be adopted for NDV encapsulation.[11] Similar difficulties were encountered for the encapsulation of adenovirus vector type 5 (Ad5). Severe deactivation of Ad5 under strongly alkaline conditions limited the synthesis of crystalline MOFs, and only amorphous Zn and 2-MIM complex polymer encapsulated Ad5 (Ad5@aZn-MIM) could be constructed under a strictly controlled concentration and molar ratio of 2-MIM/Zn^{2+}.[24] The amorphous ZIF-8 coating, however, did not stabilize the encapsulated Ad5 and even led to a more rapid loss in bioactivity than the naked virus and the amorphous aZn-MIM coating formed large agglomeration in buffer solution.[24]

Due to difficulties facing the utilization of ZIF materials toward environmentally sensitive viral antigen encapsulation, it is an important, but challenging task to seek a more effective strategy to balance the antigen stability and the ZIF-8 crystal growth on proteinaceous particles. Inactivated foot-and-mouth disease virus (iFMDV, also known as 146S due to its sedimentation coefficient), the most important vaccine antigen for FMD, was chosen as a model antigen.[25] 146S has a spherical shape with a diameter of about 30 nm [26] and is extremely unstable. When the pH deviates from its optimal range of 7.5 to 8.5 or the temperature is higher than 37 °C,[25,27] the 146S capsid will soon dissociate into its pentameric subunits, known as 12S, and lose most of its immunogenicity.[26,28] Another distinct feature of 146S is that there are numerous transition metal ion binding sites on 146S, especially the His residue at the inter-pentameric surface of the capsid.[19] Our previous study had confirmed that transition metal ions like Cu^{2+} and Ni^{2+} could reversibly spontaneously bind to 146S with high affinities and increase the stability of 146S by forming a transition metal ion bridge to link the adjacent His at the interpentameric interface of the capsid.[19] We expect that the similar affinity of His for Zn^{2+} toward the 146S surface will increase the stability of the antigen and promote the mineralization process of ZIF-8, thus providing some additional opportunity for better control of the size and morphology of the 146@ZIF-8 composite. Meanwhile, the ZIF-8 coating is expected to exert adjuvant effects benefiting from its particulate characteristics.

To this end, the synthetic conditions for ZIF-8 coating on the surface of 146S were carefully optimized by adjusting the solution pH and the 2-MIM/Zn^{2+} ratio, and adding a cationic surfactant capping agent. Then, the effects of ZIF-8 encapsulation on the structural integrity, stability, and *in vitro* and *in vivo* immune responses of 146S were evaluated. Our results showed that 146S could be successfully encapsulated into ZIF-8 at 26 °C and pH 9.0, with high encapsulation efficiency. The morphology and the particle size of 146S@ZIF-8 could be well controlled by increasing the amount of Zn^{2+} or adding cetyltrimethylammonium bromide (CTAB) in the reaction system. Under optimal conditions, single-146S nanoparticle armored with nanometer-scale crystal ZIF-8 networks were successfully prepared. The encapsulation of ZIF-8 not only enhanced the thermostability of 146S, but also significantly promoted the immune responses to 146S in the mice model without adding another immunopotentiator. Our findings provided a strategy for biomimetic mineralization of MOFs on environment-sensitive antigens and expanded the application of MOFs in vaccine delivery.

Results and discussion

Synthesis of 146S@ZIF-8

As an extremely unstable antigen, the capsids of 146S particles will dissociate rapidly into inactive pentamers (12S) or subunit proteins accompanied by the release of the encapsidated RNA at pH deviating from its optimal value (around 7.5–8.5) or at high temperature.[27,29] The pH of the 2-MIM solution for synthesizing ZIF-8 is higher than 10.0. This incompatibility of the reaction

pH is the major challenge for synthesizing 146S@ZIF-8. Therefore, finding suitable reaction pH became one of the most crucial issues. To determine the pH range in which 146S was stable in the 2-MIM solution, 146S was mixed with the 2-MIM solution of different pH values, and the loss of intact 146S was measured by high-performance size-exclusion chromatography (HPSEC) immediately. According to the HPSEC analyses, the intact 146S showed only one characteristic peak at about 10.8 min, indicating that the 146S material used for 146S@ZIF-8 synthesis was complete 146S virus particles (capsid particles with RNA inside) with high purity (Fig. 1a).[30] When the 146S solution was mixed with 0.64 M 2-MIM solution with pH 10.9, the peak at 10.8 min decreased immediately accompanied by the appearance of a new peak at about 14.8–17.5 min, which is assigned to 12S and protein subunits.[30] Based on the decrease in the peak area of the intact 146S, more than 60% of 146S particles lost their intact structure and dissociated into 12S at pH 10.9. The dissociation of 146S became less in 2-MIM solution with weaker alkalinity, and almost no dissociation was detected at pH 7.0–7.5. As the pH further decreased from 7.0 to 6.0, the stability of 146S decreased sharply again (Fig. 1b). These results suggested that 146S in 2-MIM solution was more sensitive to pH than in PBS buffer, where 146S could stabilize in the pH range from 7.5 to 8.5.[27] Therefore, ideally, 146S@ZIF-8 should be synthesized at neutral pH to avoid 146S disassociation. Unfortunately, no ZIF-8 could be formed at a pH lower than 8.5, even after 48 hours of incubation (Fig. 1c). The 2-MIM solution of pH 9.0 seems to be the lowest pH required to form ZIF-8, and at higher pH, more ZIF-8 was synthesized with a higher reaction rate. To make a compromise between 146S stability and ZIF-8 formation, the 2-MIM solution of pH 9.0 was used to explore the synthetic conditions of 146S@ZIF-8 in the subsequent experiments, although about 20% 146S would possibly disassociate at this pH.

Then, the encapsulation of 146S into ZIF-8 was investigated by mixing the pH 9.0 2-MIM solution with 146S and $ZnCl_2$ solution at a final 2-MIM/Zn^{2+} (L/Zn) ratio of 64 : 1. The formation process of 146S@ZIF-8 was judged by measuring the decrease of the 146S content remaining in the supernatant of the reaction system by HPSEC. As shown in Fig. 2a, the 146S signal peak gradually decreased with the reaction. Less than 10% of the original amount of 146S was left at 10 hours. Then, the reaction was terminated by separating the formed 146S@ZIF-8 precipitation from the reaction system. There were obvious peaks corresponding to 12S on the chromatograms at 0 and 2 hours of reaction. Afterward, no 12S was detected after 4 hours. It indicated that some 146S disassociated into 12S during the reaction, and 12S was also encapsulated into ZIF-8.

SDS-PAGE was further applied to monitor the reaction process. The 146S capsid showed three distinct bands with molecular weights of about 25 kDa, corresponding to the three subunits (VP1, VP2, and VP3), respectively (Fig. 2b, lane 9). In the first 8 hours, the bands gradually faded with the progress of the reaction and became almost undetectable at 10 hours (Fig. 2b, lanes 1–5), indicating the complete encapsulation of 146S. This result was consistent with the HPSEC analysis.

Since there is single-strand RNA encapsidated in the 146S capsid, agarose gel electrophoresis (AGE) was also applied to monitor the reaction process. On the AGE image, the intact 146S showed a smear nucleic acid band, which can roughly be divided into two fractions. The larger size band (migrating slowly, marked by the blue box in Fig. 2b) was considered to correspond to the RNA encapsulated in the intact 146S capsids. Since the HPSEC analysis proved that the 146S particles are complete virus particles with high purity, the nucleic acid substances showing a smaller size band on AGE (migrating faster, marked in the orange box in Fig. 2b) were speculated to be released during electrophoresis, which might cause dissociation of part of the 146S capsid. During 146S@ZIF-8 synthesis, the brightness of the larger size band decreased gradually in the early stage, indicating a decrease of intact 146S in the supernatant. The brightness of the smaller size band increased slightly during the first 4 hours, indicating the dissociation of 146S and release of the nucleic acids. The brightness of the smaller size remained unchanged till the end of the reaction, suggesting that the released nucleic acids were not, at least partially, encapsulated in 146S@ZIF-8.

By making closer observation of the HPSEC chromatograms, an unknown peak at 18.0 min was observed at 4 hours and afterward became higher with the progress of the reaction (Fig. 2a). However, this peak did not appear in the disassociated 146S sample. No protein and nucleic band were observed on the electrophoretic images of the supernatant at 10 hours after reaction (Fig. 2b). Therefore, this peak was attribute to unknown small-molecular by-products formed in the synthesis process, rather than a component of 146S.

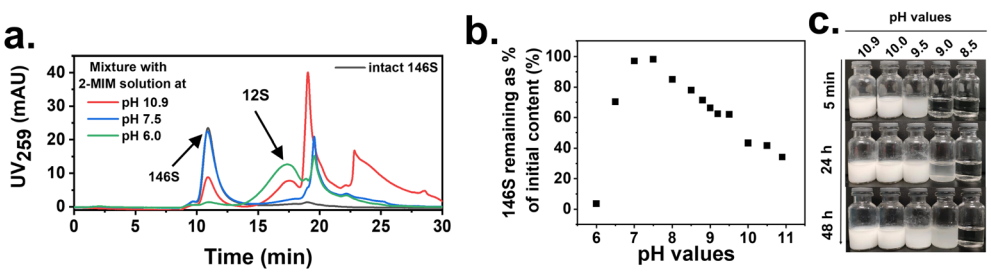

Fig. 1 Exploration of the pH window for the synthesis of 146S@ZIF-8. (a) HPSEC of intact 146S and 146S mixed with 0.64 M 2-MIM solution of pHs 10.9, 7.5, and 6.0. The characteristic peak of the intact 146S (black line) and that in pH 7.5 2-MIM (blue line) overlapped. (b) Quantitative plotting of 146S remaining as % of the initial content after mixing with 0.64 M 2-MIM solution of different pHs as measured by HPSEC. (c) Pictures of the synthesized ZIF-8 in 0.64 M 2-MIM solution at different pH and time points.

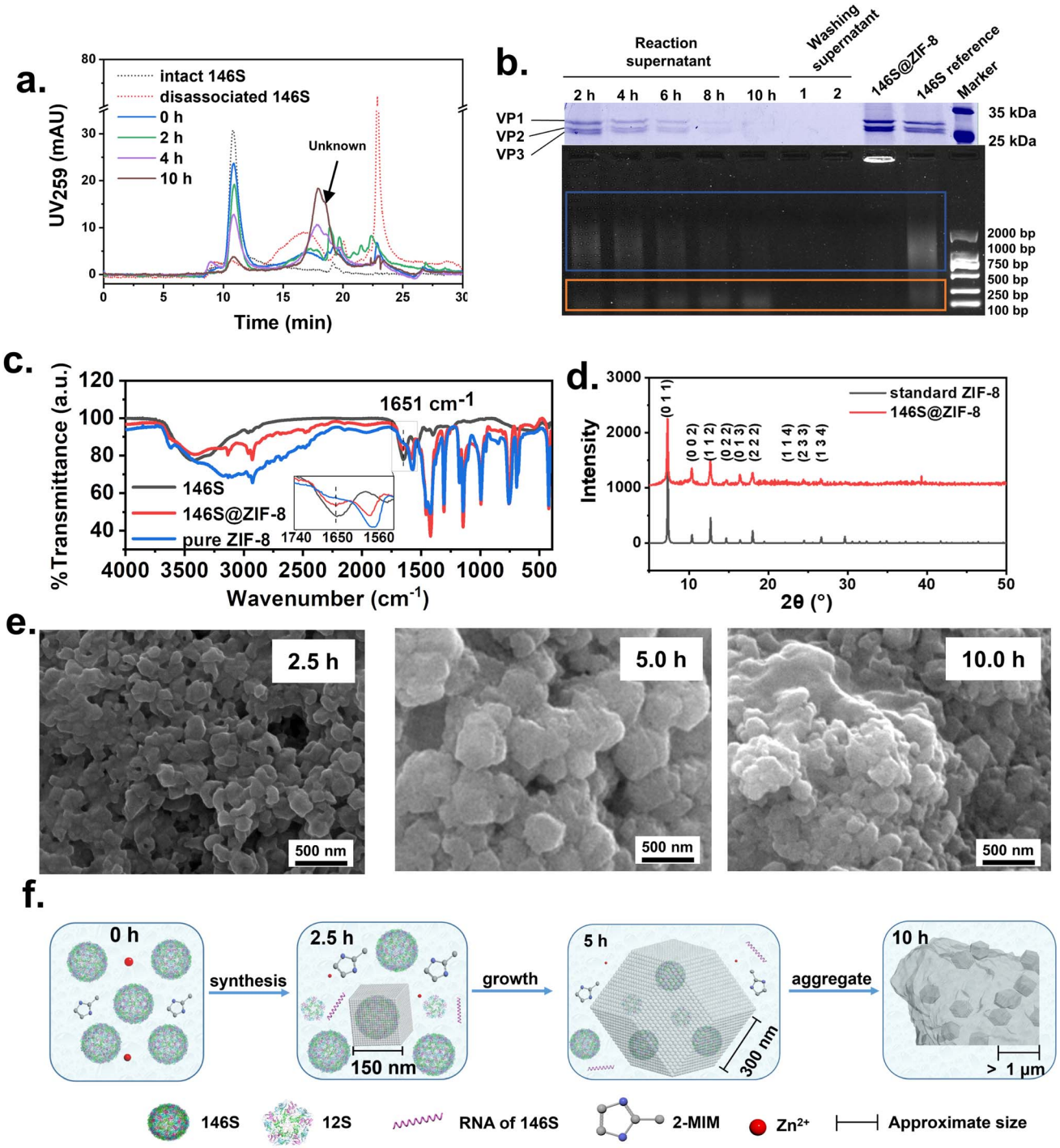

Fig. 2 The synthesis process and characterization of 146S@ZIF-8. Monitoring of the preparation process of 146S@ZIF-8 by (a) HPSEC and (b) SDS-PAGE and agarose gel electrophoresis. Lanes 1–5: reaction supernatant of 2, 4, 6, 8, and 10 hours; lanes 6 and 7: washing supernatant; lane 8: suspension of synthesized 146S@ZIF-8; lane 9 and M: 146S reference and marker. (c) FT-IR and (d) PXRD spectra of the synthesized 146S@ZIF-8. The PXRD map of standard ZIF-8 was from the Cambridge Crystallographic Data Centre.[39] (e) The SEM images of 146S@ZIF-8 obtained at different reaction times. (f) The schematic diagram for the formation process of 146S@ZIF-8.

To further verify the successful encapsulation of 146S in 146S@ZIF-8, the synthesized products (white precipitate) were collected and washed twice to remove the unreacted components. No 146S was detected in the washing solution by SDS-PAGE and AGE (Fig. 2b, lanes 6–7), and there were strong subunit bands of 146S in the re-suspended precipitation, which confirmed that 146S had been successfully encapsulated in ZIF-8 (Fig. 2b, line 8). Meanwhile, a strong nucleic acid band was observed on the AGE of the 146S@ZIF-8 sample, though the particle was too large to migrate in the AGE-gel. This

phenomenon also appeared when the micro-RNA was encapsulated into MOFs.[31]

Characterization of 146S@ZIF-8

The structure of synthesized 146S@ZIF-8 was identified by collecting products after 10 hours of reaction and characterized by Fourier transform infrared spectroscopy (FT-IR) and powder X-ray diffraction (PXRD). Compared with reported data of ZIF-8[24,32] and pure ZIF-8 (synthesized using 2-MIM without adjusting the pH value), there was no difference in the fingerprint region in FT-IR. The peaks ν/cm^{-1} 1110 (C–N) and 1580 (C=N) confirmed the existence of the imidazole ring. The peak at 420 cm^{-1} revealed the corresponding Zn^{2+} and N atoms. In addition, the characteristic absorption peak ν/cm^{-1} 1651 (C=O) occurred in the synthesized 146S@ZIF-8, indicating successful encapsulation of 146S (Fig. 2c). The correct crystal structure of 146S@ZIF-8 was also verified by PXRD analysis (Fig. 2d).[33]

The size and morphology of 146S@ZIF-8 were observed by using a scanning electron microscope (SEM). The particles formed after 2.5 hours of reaction showed an irregular cubic morphology with an average diameter of about 150 nm (Fig. 2e). Numerous rough surface particles with an average diameter of 300 nm were obtained at 5 hours. Further prolonging the reaction to 10 hours, the particles aggregated to form "cloud-like" structures.[34]

The pH and L/Zn ratio play essential roles in the synthesis of ZIF-8. Generally, much excess 2-MIM ligands and high pH are beneficial to form ZIF-8 with a small size and high purity, because the large amount of deprotonated 2-MIM can rapidly coordinate with Zn^{2+} to complete the nucleation and crystal growth.[33] A L/Zn ratio of 64 : 1 was adopted in this work, under which ZIF-8 with a size of about 85 nm was synthesized within 5 min.[35,36] The relatively low solution pH was considered one of the main causes for the formation of the "cloud-like" structures in our work. However, the pH of 2-MIM had to be adjusted to 9.0 to avoid severe dissociation of 146S (Fig. 1). Therefore, the deprotonation of 2-MIM was inhibited, and the nucleation rate was hindered. On the other hand, due to a large number of His residues on 146S (about 1200 His per 146S), Zn^{2+} can be adsorbed on their surface to form nucleation by coordinate interaction, besides commonly reported electrostatic interactions.[22,37] Therefore, ZIF-8 mainly grew on the 146S surface to form 146S@ZIF-8 with a size of about 150 nm at the early stage (*ca.* first 2 hours). This process was accompanied by a small amount of 146S dissociating into 12S due to the alkaline environment. With the consumption of 146S in solution (*ca.* 2–5 hours), more 146S and a fraction of 12S were wrapped into ZIF-8, and the size of 146S@ZIF-8 gradually increased to about 300 nm after 5 hours of reaction. Compared with 146S@ZIF-8 at 2.5 hours, 146S@ZIF-8 at 5 hours showed a heterogeneous size.

According to Ostwald ripening theory, the large crystals tend to grow larger at the expense of the smaller crystals to minimize the surface free energy.[34,38] However, as the reaction time further prolonged to 10 hours, the average particle size remained approximately the same but "cloud-like" aggregation appeared (Fig. 2e). We speculated that the Ostwald ripening was limited, due to the following two special aspects. Firstly, unlike usual proteins, the 146S particles are sphere particles with sizes as large as 30 nm. The large interfacial tension between the 146S particles and the surrounding ZIF-8 network makes the dissolution of smaller 146S@ZIF-8 energetically unfavorable.[23] Secondly, the tight coordinating connection between Zn^{2+} and His residues might further increase the difficulty of dissolution of the small ZIF-8 crystal (discussed in detail later). As a result, the 146S@ZIF-8 particles tend to minimize the system energy by forming sub-micron aggregates, rather than increasing the particle size, during the aging phase (*ca.* 5–10 hours). The whole process and possible synthesis mechanism are schematically depicted in Fig. 2f.

Release behavior and structural integrity of 146S in 146S@ZIF-8

Maintaining the structural integrity of 146S is crucial during the synthesis process of 146S@ZIF-8 to ensure the production of antibodies and sensitization of lymphocytes. According to HPSEC and SDS-PAGE analyses, most of the 146S particles were encapsulated, either in complete virus particle form or in dissembled form (12S or subunits) and RNA. To verify the integrity of 146S encapsulated in 146S@ZIF-8, we firstly tried to lysate 146S from 146S@ZIF-8 by ethylene diamine tetraacetic acid (EDTA) treatment. Upon the addition of 0.1 M EDTA (final concentration), the turbid mixture solution gradually became clear. The lysate solution was centrifuged, and the supernatant was analyzed by TEM, HPSEC, and SDS-PAGE. There was a small amount of intact 146S observed in TEM (Fig. 3a). However, no 146S signal peak was detected by HPSEC even after 24 hours of treatment (Fig. S1†). A similar result was also observed from the SDS-PAGE analysis. No protein band was present in the supernatant (Fig. 3b, lane 2), and it was useless when increasing the EDTA concentration to 0.5 M and prolonging the treating time to 72 hours. Then, the residual left in the vial after removing the supernatant was re-suspended by adding PSB with a half volume of the lysate solution and analyzed by SDS-PAGE. Obvious subunits of 146S with gray-scale approximately as twice as those in the lysate solution were observed (Fig. 3b, lane 1 and lane 3). These results suggested that there were some non-soluble substances remained after EDTA treatment. Most of the 146S particles existed in these substances, but they were too small to be visibly seen.

To identify whether the non-soluble substances in the lysate were the 146S aggregation or small 146S@ZIF-8, the precipitates were washed thoroughly with ultrapure water and characterized by SEM and Energy Dispersive Spectroscopy (EDS). Surprisingly, a large number of spheroid particles with a diameter of 30–40 nm were observed in the SEM image (Fig. 3c). And the EDS images showed a uniform distribution of C, N, O, and Zn signals (Fig. S2†), indicating the co-existence of the ZIF-8 network and protein components. The lysing process was also characterized by dynamic light scattering (DLS). The size of empty ZIF-8 without 146S gradually decreased to less than 1 nm after 24 hours when treated with EDTA (Fig. 3d). While the particle size of 146S@ZIF-8 decreased slightly after adding EDTA, particles

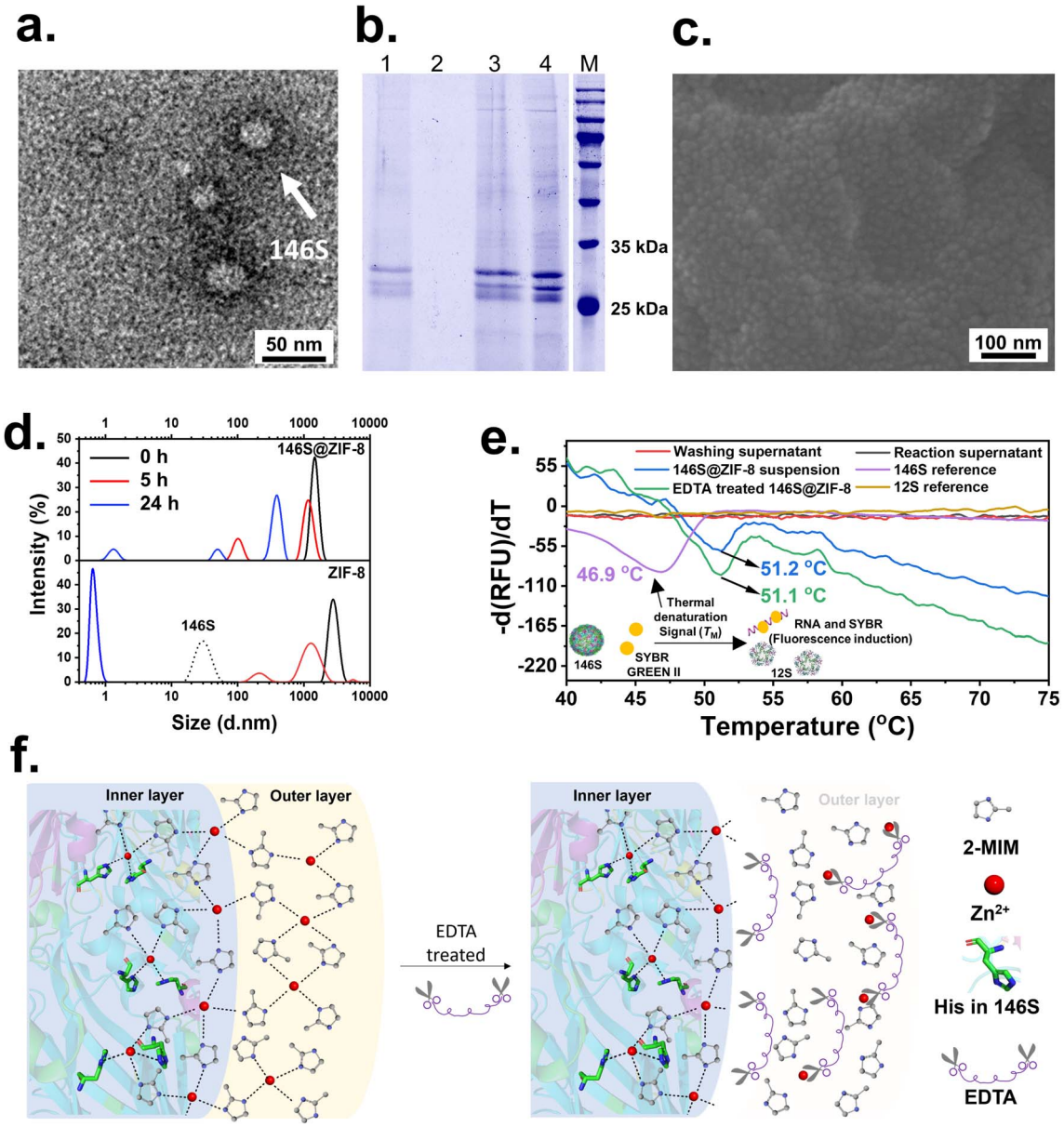

Fig. 3 Release of 146S from 146S@ZIF-8 by EDTA and thermostability analysis. (a) The TEM image of 146S particles released from 146S@ZIF-8 after EDTA treatment. (b) SDS-PAGE analyses of the EDTA treatment process. Lane 1: the lysate mixture of 146S@ZIF-8; lane 2: the supernatant of the lysate mixture; lane 3: the insoluble substances after EDTA treatment re-suspended into PSB with a half volume of the lysate solution; lane 4 and M: 146S reference and marker. (c) SEM image of the insoluble substances after EDTA treatment. (d) Change in the size distribution of empty ZIF-8 and 146S@ZIF-8 during EDTA-treatment measured by DLS. (e) DSF analyses of 146S samples in different stages and the derived T_m values are marked. (f) Schematic illustration of the 146S@ZIF-8 and EDTA-induced exfoliation process. In the inner layer near the vicinity of the 146S particle, the existence of His-Zn-MIM coordination enabled its resistance to EDTA. In the outer layer, there was only Zn^{2+}-MIM coordination that was susceptible to EDTA treatment.

with a diameter of about 100 nm appeared at 5 hours. When the reaction reached 24 hours, the particle size further decreased, and particles with a diameter of about 49 nm were observed, which was consistent with the SEM results (Fig. 3c). It suggested that the remained nanoparticles in the lysate after 24 h EDTA treatment were a thin shell of ZIF-8 with 30 nm 146S as the core inside. It was extensively reported that the protein coated with ZIF-8 can be recovered in high yield by EDTA treatment.[11,22,40] For 146S@ZIF-8, however, all above phenomena suggested that though EDTA treatment exfoliated a large fraction of the ZIF-8 network. There was still a thin ZIF-8 shell closely surrounding the complete or dissociated 146S viral particles which could not be released.

To further confirm the structural integrity of 146S in 146S@ZIF-8, we turned to use differential scanning fluorescence (DSF) analytical technology. This method has been developed and employed as a sensitive tool to analyze the transition temperature (T_m) associated with 146S dissociation,

which is a thermo-dynamic parameter sensitive to the structural state of biomolecules. The mechanism for DSF analysis for 146S is schematically illustrated in Fig. 3e. Upon 146S dissociation during heating, the RNA will be released and specifically bind to the fluorescent probe SYBR Green II, thus triggering a strong fluorescence signal.[41,42] The T_m is derived from the maximum value of the first derivative curve of the fluorescence curve against temperature, which corresponds to the temperature inducing 50% dissociation of intact 146S. Since only the intact 146S shows a distinct thermal denaturation process during heating, 12S does not show fluorescent signals during measurement. Therefore, the presence of the dissociative signal thus can be a unique indicator of the existence of complete 146S (capsid particles with RNA inside). The T_m value of intact 146S was about 46.9 °C (Fig. 3e), and there was no DSF signal detected in the reaction supernatant and the washing solution (Fig. 3e). These further confirmed that no detectable intact 146S was left after 146S@ZIF-8 synthesis. In contrast, the synthesized 146S@ZIF-8 showed not only strong DSF signals but also the T_m value (51.2 °C) was about 4.3 °C higher than that of naked 146S, indicating the structural integrity and enhanced thermostability of 146S. More importantly, the EDTA-treated sample also exhibited strong DSF signals with a T_m value of 51.1 °C. This strongly suggested that though a few dissociations of 146S took place during 146S@ZIF-8 synthesis, most of the 146S particles are complete virus particles in the synthetic nanoparticles, even after EDTA treatment.

Fig. 3f schematically illustrates the possible structure of 146S@ZIF-8 and the EDTA-induced dissolution process. The coordinate and electrostatic interactions between Zn^{2+} and 146S will attract a large amount of Zn^{2+} to cause local high-concentration nucleation, as discussed above. As a tetradentate metal, the Zn^{2+} in the vicinity of 146S particles will possibly form coordination interactions with the His on the 146S surface and the MIM^-, thus forming a unique His-Zn-MIM coordination (Fig. 3f, the inner layer). Meanwhile the Zn^{2+} apart from 146S will coordinate exclusively with MIM^- to form a Zn-MIM coordination (Fig. 3f, the outer layer), as well as some empty ZIF-8 without 146S being wrapped.

The stability constants of Zn^{2+} with methylimidazole ($10^{2.44}$) and His ($10^{6.60}$) show that His–Zn interaction is about 14 454-times more stable than the Zn-MIM coordination. Moreover, there are five donor atoms in His, which allow the exogenously added His to replace the MIM^- in the skeleton of ZIF-8 *via* the ligand substitute.[43] This ligand substitute protocol was recently applied to form a nanocoating on amorphous Ad5@aZn-MIM. It was discovered that at His exchange equilibrium, the molar fraction of incorporated His to MIM^- reached 13.39%, and the introduction of the His layer significantly reduced the hydrolysis of the Zn-MIM complex and improved the thermostability of Ad5.[24] The coordination of exogenously added His onto Ad5@aZn-MIM did not alter its EDTA sensitivity. The effect on the thermostability of Ad5 disappeared upon adding EDTA due to the ablation of Zn coordination.

Compared with the intramolecular linkage between exogenously added His, the *in situ* formed coordination that linked endogenous virus His with the Zn^{2+} and 2-MIM seems more rigid. When the synthesized 146S@ZIF-8 with a high degree of crystallinity was treated with EDTA, only the outer layer of 146S@ZIF-8 and empty ZIF-8 could be dissolved, while the very thin inner layer surrounding 146S could not be exfoliated due to the tight coordination. By comparing the size of 146S particles of about 30 nm (Fig. 3d) and the insoluble substances left after EDTA treatment (*ca.* 30–40 nm based on the SEM image and about 49 nm based on DLS), it can be reasonably speculated that the insoluble substances were armored single-146S MOFs that surround each 146S particle with a ZIF-8 network of a few nanometers thick. This armor network endowed the enclosed 146S with a significantly improved stability. Even after EDTA treatment, the integrity of 146S in this network was well preserved, and the stabilization effect was retained, as confirmed by the T_m as high as 51.1 °C.

Besides the stabilization effect endowed by the MOF amour composed of His-Zn-MIM crystal networks, the Zn^{2+} that can coordinate with the His of virus will also form a transition metal ion bridge to link the adjacent His at the interpentameric interface of 146S,[19] thus further increasing the stability of 146S. Taking all these aspects together, the unique molecular properties of 146S and its coordination interactions with Zn^{2+} endowed 146S@ZIF-8 with extraordinary stability against both EDTA treatment and heat dissociation.

Optimizing the morphology and size of 146S@ZIF-8

We have demonstrated that 146S can be successfully encapsulated into ZIF-8 by tuning the pH to make a compromise between ZIF-8 synthesis and antigen stability. However, the large size and poor morphology of 146S@ZIF-8 may hinder its uptake by antigen-presenting cells (APCs)[20] and targeting lymph nodes.[14] Therefore, the size and morphology of 146S@ZIF-8 were further optimized to make it suitable for vaccine use in this part.

According to the mechanism of 146S@ZIF-8 formation (Fig. 2), the reaction time plays a crucial role in controlling the particle size and morphology. The longer the reaction time, the more aggregation. Therefore, we first tried to accelerate the reaction rate by using a higher concentration of Zn^{2+}. Specifically, the L/Zn ratio in the reaction system was adjusted from initially used 62 : 1 ($1\times Zn^{2+}$) to 31 : 1 ($2\times Zn^{2+}$), 21 : 1 ($3\times Zn^{2+}$), and 16 : 1 ($4\times Zn^{2+}$) by keeping constant the 2-MIM amount. As expected, the 146S encapsulation process was significantly increased, such that the time for 90% 146S encapsulation was shortened from 10 hours ($1\times Zn^{2+}$) to 90 min ($2\times Zn^{2+}$), 12 min ($3\times Zn^{2+}$) and 2 min ($4\times Zn^{2+}$), respectively, according to HPSEC analyses (Fig. 4a and S3†). The increase in Zn^{2+} concentration also led to significant changes in the morphology of 146S@ZIF-8. 146S@ZIF-8($2\times Zn^{2+}$) still showed the "cloud-like" structures (Fig. 4b). 146S@ZIF-8($3\times Zn^{2+}$) showed two different structures; besides the cube-shape 146S@ZIF-8 crystal containing O, C, N, and Zn elements, there were flower-like shape substances containing only C, N, and Zn elements, which were some by-products without containing protein (analyzed by EDS, Fig. S4†). 146S@ZIF-8($2\times Zn^{2+}$) and 146S@ZIF-8($3\times Zn^{2+}$) exhibited some additional absorption peaks that did not fully

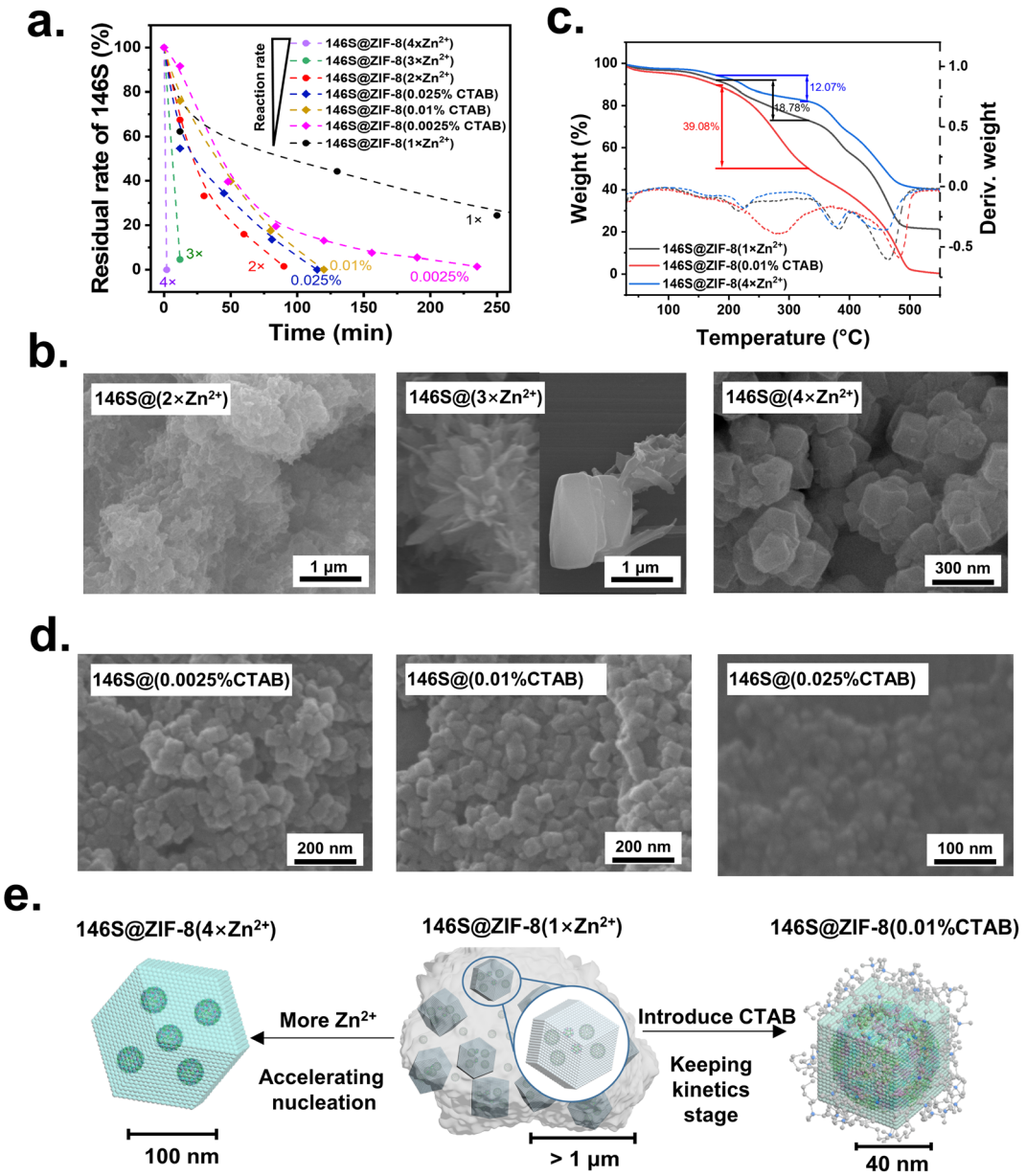

Fig. 4 Optimization of the morphology of 146S@ZIF-8. (a) Encapsulation rate of 146S during the preparation of each ZIF-8 under different conditions. The complete reaction curve of 146S@ZIF-8(1×Zn^{2+}), including the depletion process of 146S from 250 min to 10 hours, is provided in Fig. S3.† (b) The SEM images of 146S@ZIF-8 synthesized by adjusting the Zn^{2+}/2-MIM molar ratios from initial 1 : 62 (1×Zn^{2+}) to 1 : 31 (2×Zn^{2+}), 1 : 21 (3×Zn^{2+}) and 1 : 16 (4×Zn^{2+}). (c) Identification of 146S@ZIF-8 synthesized under different conditions using TGA. (d) The SEM images of 146S@ZIF-8 synthesized by adding 0.0025% (w/v), 0.01% (w/v) or 0.025% (w/v) CTAB. (e) Schematic illustration of the structure conjecture of 146S@ZIF-8 with different sizes and morphologies, as well as the main manipulating mechanism of 4×Zn^{2+} and CTAB strategy. 146S@ZIF-8(1×Zn^{2+}): cloud-like aggregate composed of ZIF-8 particles with encapsulated 146S and 12S; 146S@ZIF-8(4×Zn^{2+}): about 146 nm rhombic dodecahedron with multi-146S being encapsulated; 146S@ZIF-8(0.01% CTAB): about 49 nm cubes with single 146S encapsulated inside and CTAB adsorbed on its surface.

match with the standard ZIF-8 card on PXRD spectra, which were probably due to the existence of by-products such as $Zn(OH)_2$ (marked with triangles in Fig. S5,† JCPDS: 01-089-0138).[34] 146S@ZIF-8(4×Zn^{2+}) prepared with the L/Zn ratio at 16 : 1 showed a single rhombic dodecahedral morphology with an average diameter of about 146 nm. PXRD analysis (Fig. S5†) confirmed a high degree of crystallinity, as its absorption peaks were consistent with the standard ZIF-8 card. When ZIF-8(1×Zn^{2+}) to ZIF-8(4×Zn^{2+}) was prepared under the same conditions without 146S, the peaks of by-products also occurred. This suggested that the existence of 146S is conducive to the synthesis of ZIF-8 with high crystallinity (Fig. S6†). Besides improvement in the morphology, the significantly shortened reaction time (only 2 min) was also beneficial to avoiding the dissociation of 146S. Thermogravimetric analysis (TGA) showed that the mass ratio of 146S in 146S@ZIF-

8(1×Zn^{2+}) and 146S@ZIF-8(4×Zn^{2+}) was 18.78% and 12.70%, respectively (Fig. 4c). Due to more nucleation, 146S@ZIF-8(4×Zn^{2+}) showed a slightly lower 146S content.

Introducing surfactants with long alkyl chains into the reaction system is another strategy to reduce the size of ZIF-8. It was reported that the cationic surfactant CTAB can adsorb on the fast-growing crystal surfaces and thus act as a capping agent to hinder the growth of ZIF-8.[44] Here, a different amount of CTAB was added to the reaction system. The time for 90% 146S encapsulation was shortened from 10 hours to 140 min, 97 min, and 90 min (Fig. 4a), with the average diameters of the synthesized 146S@ZIF-8 decreased to 57 nm, 49 nm, and 30 nm (Fig. 4d), respectively, by adding 0.0025% (w/v), 0.01% (w/v), and 0.025% (w/v) of CTAB. Meanwhile, the shapes of 146S@ZIF-8 changed from a typical rhombic dodecahedron to a truncated cubic morphology with the increase of CTAB concentration (Fig. 4d), as the inhibitory effect of CTAB on the growth of the {100} facets was more profound.[45] Considering that the complete 146S viral particles have a diameter of about 30 nm (Fig. 3d), it is reasonable to suppose that there was a single 146S viral particle inside per 146S@ZIF-8(0.01% CTAB) (Fig. 4d). The introducing of the CTAB surfactant modulated the ZIF-8 growth mechanism and significantly accelerated the reaction rate. Therefore, the dissociation of 146S during 146S@ZIF-8 synthesis was largely reduced, as confirmed by HPSEC analysis in which there was no 12S detected (Fig. S7†).[46] 146S@ZIF-8(0.01% CTAB) also exhibited a high degree of crystallinity according to PXRD analysis (Fig. S5†). Meanwhile, the DSF mensurate of the synthetic 146S@ZIF-8(0.01% CTAB) further proved the retention of the complete structure of the 146S viral particle (Fig. S8†). All these results demonstrated that 146S@ZIF-8(0.01% CTAB) was composed of only single 146S armored with a thin layer of the ZIF-8 MOF. Previously, the growth of crystal ZIF-8 on a single bioparticle seems only reported on TMV, which is a highly anisotropic rod shape virus.[13] The synthesis of crystal structure ZIF-8 on small isotropic materials, such as the polio virus at about 30 nm, was considered very difficult due to the high stress–strain induced by the MOF shell growth on it.[23] The successful synthesis of 146S@ZIF-8(0.01% CTAB) composed of single 146S viral nanoparticles without altering the structural integrity is therefore significant for biomimetic mineralization of MOFs on environment-sensitive antigens.

Thermogravimetric analysis (TGA) has been widely used to determine the proportion of loaded drugs in ZIF-8 particles.[14,47] Here we estimated the loading capacities of 146S in three ZIF-8 synthesized under different conditions by TGA. As presented in Fig. 4c, there was a significant weight loss from 200–350 °C, which was attributed to the decomposition of the protein. Then a sharp decrease at 400–450 °C was consistent with the decomposition of ZIF-8.[13] Accordingly, the 146S loading capacity in 146S@ZIF-8(1×Zn^{2+}), 146S@ZIF-8(4×Zn^{2+}) and 146S@ZIF-8(0.01% CTAB) was roughly estimated to be about 18.78%, 12.07%, and 39.08%, respectively. The 146S loading capacity in 146S@ZIF-8(0.01% CTAB) was not only higher than that in the other two 146S@ZIF-8 but also significantly higher than most of the reported values of bioparticle@ZIF-8, such as enzyme (Gox, 10%),[6] virus (TMV, 10% and adenovirus, 7.5%)[13,24] and other proteins (OVA, 7%).[48] The high loading capacity further suggested that 146S@ZIF-8(0.01% CTAB) is composed mainly of single 146S viral particle armored with a very thin layer of the MOF.

It was reported that the synthesis of ZIF-8 goes through the kinetic stage to the final thermodynamic stage, during which square particles with larger surfaces and energy transform into rhombic dodecahedral particles.[33,38] The high Zn^{2+} strategy was considered to mainly promote the nucleation on the 146S surface and limit the overgrowth of the thermodynamic product. Therefore, about 146 nm rhombic dodecahedron was formed with multiple 146S encapsulated inside each ZIF-8 particle. Meanwhile for the CTAB strategy, the reaction was possibly kept in the kinetic stage as the surface energy can be effectively reduced by adsorbing CTAB,[44] thus about 49 nm cubes nanoparticle and CTAB adsorbed on its surface were obtained. Fig. 4e schematically illustrates the structure conjecture of 146S@ZIF-8 with different sizes and morphologies, as well as the main manipulating mechanism of a high amount of Zn^{2+} and CTAB strategies. 146S@ZIF-8(4×Zn^{2+}) and 146S@ZIF-8(0.01% CTAB) synthesized under optimal conditions all exhibited a high degree of crystallinity, enhanced 146S thermostability, and high EDTA-tolerance (Fig. S8†).

Altogether, adjusting the L/Zn ratio or introducing CTAB was effective in regulating the morphology and size of 146S@ZIF-8. Especially, single-146S nanoparticles armored with a nanometer-scale MOF network could be formed when applying CTAB. The much-reduced size, improved morphology, and extraordinary stability of 146S@ZIF-8(4×Zn^{2+}) and 146S@ZIF-8(0.01% CTAB) are expected to endow the nano-vaccines with a great potency.

In vitro cellular uptake

The ZIF-8 material could generally promote transmembrane transport,[49] and thus the *in vitro* cellular uptake of the synthesized 146S@ZIF-8(1×Zn^{2+}), 146S@ZIF-8(4×Zn^{2+}), and 146S@ZIF-8(0.01% CTAB) by DC 2.4 cells was evaluated, and the results are presented in Fig. S9† and 5a. Compared with naked 146S, the antigen uptake efficiencies in 146S@ZIF-8(4×Zn^{2+}) and 146S@ZIF-8(0.01% CTAB) groups were 8.9 and 2.6-times higher, respectively, and 146S@ZIF-8(4×Zn^{2+}) showed the highest efficiency. 146S@ZIF-8(1×Zn^{2+}), however, showed decreased uptake efficiency. Native 146S, 146S@ZIF-8(1×Zn^{2+}), and 146S@ZIF-8(0.01% CTAB) all have negative surface ζ-potential, and at the same time ZIF-8(4×Zn^{2+}) shows a significant positive charge of 6.94 mV (Fig. 5b). This positive charge could promote the endocytosis of particles by DC2.4 cells.[50] 146S@ZIF-8(1×Zn^{2+}) had a large size and low surface ζ-potential (−19.8 mV), and its uptake by DC2.4 cells was therefore hindered. In addition, the uptake efficiency was also affected by the size of the antigens.[20] 146S@ZIF-8(4×Zn^{2+}) and 146S@ZIF-8(0.01% CTAB) have average diameters of 146 and 49 nm, well within the most appropriate uptake size range (*ca.* 20–200 nm) for APCs,[20] and therefore showed the highest uptake efficiency. It was worth noting that 146S@ZIF-8(0.01% CTAB) having the

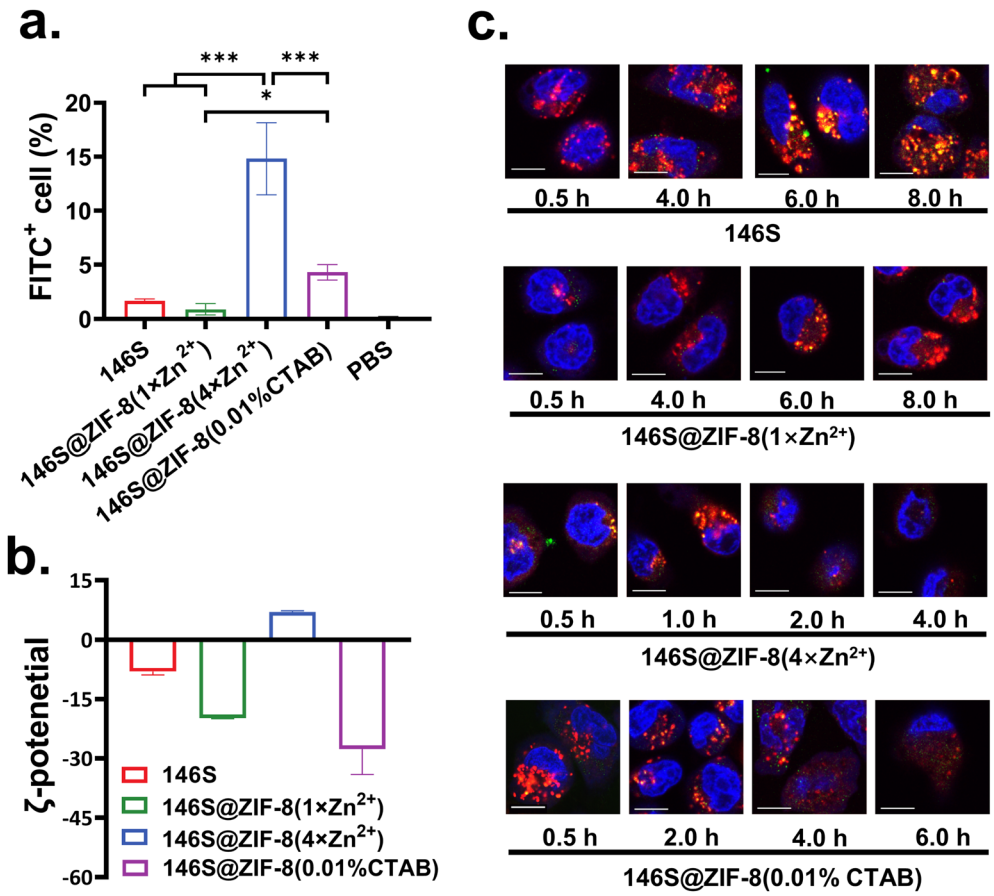

Fig. 5 (a) Effects of the ZIF-8 encapsulation on the *in vitro* uptake efficiency of 146S by DC2.4 cells ($n = 3$). The DC2.4 cells were co-cultured with FITC-labeled 146S or 146S@ZIF-8 for 4 hours, and the uptake efficiency was measured using flow cytometry. The asterisks indicate significant differences (*$P < 0.05$, **$P < 0.01$, and ***$P < 0.001$). (b) The ζ-potential of 146S and 146S@ZIF-8 measured using DLS. (c) Representative confocal laser scanning images of DC2.4 cells co-cultured with 146S or 146S@ZIF-8. The 146S antigen, nuclei, and lysosomes were labeled with FITC (green), DAPI (blue), and LysoTracker Red (red), respectively. Scare bar, 10 μm.

lowest surface charge (−27.7 mV) also showed about 2.6-times higher uptake efficiency than naked 146S. The presence of CTAB on the surface of 146S@ZIF-8(0.01% CTAB) might promote the transmembrane transport of the MOF particles. It was reported that the modification of poly(lactic-*co*-glycolic acid) nanoparticles with CTAB significantly enhanced drug transmembrane transport by reducing the barrier effect of cell membranes.[51]

Another significant advantage of ZIF-8 for antigen delivery was promoting the escaping ability from lysosomal, due to the cleavage of ZIF-8 in the acidic environment of lysosomal and release of Zn^{2+} and 2-MIM, resulting in lysosomal disruption by the proton sponge effect.[14,15,52] As shown in Fig. 5c, the encapsulation of 146S in ZIF-8 promoted escaping ability. The antigens were marked with green dyes, the lysosomes were marked with red dyes, and the nuclei were marked with blue dyes to locate cells. For naked 146S, a few 146S particles were transported into the cells in 0.5 hours, and it still showed the strongest co-localization of antigens and lysosomes after incubating for 8 hours, which indicated the great difficulty of escaping from the lysosome. The strongest co-localization for 146S@ZIF-8(1×Zn^{2+}), 146S@ZIF-8(4×Zn^{2+}) and 146S@ZIF-8(0.01% CTAB) was at about 6 hours, 1 hour and 2 hours, respectively. After the strongest co-localization, the separation of antigens and lysosomes can be seen in each group, which indicated rapid escape from the lysosome.

Taken together, the results indicated that the encapsulation of ZIF-8 with appropriate size and surface properties could promote cell uptake and lysosomal escape, which is important for its entry into lymphocytes *in vivo* and triggering subsequent immune responses.[53] Although all 146S@ZIF-8 particles are pure phase crystals, the better performance of 146S@ZIF-8(4×Zn^{2+}) and 146S@ZIF-8(0.01% CTAB) than 146S@ZIF-8(1×Zn^{2+}) proves that the appropriate size and surface properties of the MOF particles will play essential roles in the immune activity of the vaccine.

In vivo immunization

146S@ZIF-8(4×Zn^{2+}) and 146S@ZIF-8(0.01% CTAB) have been proven to promote the cell uptake and lysosome escape of 146S. Considering the tight interaction of 146S and ZIF-8 (Fig. 3), it needs to be further explored whether the coated 146S can be

released from ZIF-8 *in vivo* and induce immune responses. Therefore, an animal experiment was carried out to evaluate the *in vivo* immune activities of 146S@ZIF-8. Mice were subcutaneously immunized with 146S@ZIF-8($1\times Zn^{2+}$), 146S@ZIF-8($4\times Zn^{2+}$), or 146S@ZIF-8(0.01% CTAB), and naked 146S and ZIF-8 without antigens were used as a control.

IgM is the first antibody produced by the body after being stimulated by antigens, which has strong cytotoxicity and cytolytic activity to resist intravascular infection. IgM usually reached the highest level in 1–2 weeks post immunization, and kept stable within a certain period of time.[54–56] The 146S-specific IgM antibody in serum 14 days post primary immunization is presented in Fig. 6a. The IgM antibody induced by 146S@ZIF-8(0.01% CTAB) and 146S@ZIF-8($4\times Zn^{2+}$) was 2.0 times and 1.5 times higher than by naked 146S, and the enhancement effect was more significant after boosted immunization (Fig. S10†), suggesting better antiviral activity. ZIF-8 without an antigen induced very weak IgM antibody reactions, and values elicited by primary and boosted immunization remain unchanged. It may be interfered by the non-specific reactions in the measurement process.

The 146S-specific IgG titers of the immunized mice after 28 days were measured. The results showed that the immunization with 146S@ZIF-8($4\times Zn^{2+}$) and 146S@ZIF-8(0.01% CTAB) induced antibody titers about 10 times higher than that induced by naked 146S ($P < 0.001$). There was no significant difference in IgG titers between these two groups. The immunization of 146S@ZIF-8($1\times Zn^{2+}$), however, induced even slightly lower IgG titers than naked 146S, without a statistical difference between them (Fig. 6b). The specific IgG antibody was not detectable (titer < 20) in the serum of mice immunized with ZIF-8, which proved that ZIF-8 without an antigen could not activate the immune system. Large size and poor dispersity are two of the factors limiting the adjuvant effect of the ZIF-8 materials, and more severe dissociation of 146S during a long-term encapsulation process was considered another critical cause for the relatively low efficiency of 146S@ZIF-8($1\times Zn^{2+}$), as it was well known that the dissociation product 12S has almost no immunogenicity.[57] The titers of IgG subtypes (IgG1 and IgG2a) showed a similar trend to the IgG titers, that 146S@ZIF-8($4\times Zn^{2+}$) and 146S@ZIF-8(0.01% CTAB) induced a higher level of IgG1 and IgG2a titers (Fig. S11†). The IgG1/IgG2a ratio reflects the tendency of Th2/Th1 immune responses,[58] and all of the four groups have an IgG1/IgG2a ratio higher than 1, indicating the tendency of Th2 immune responses. Among them, the 146S@ZIF-8($4\times Zn^{2+}$) group showed the highest IgG1/IgG2a ratio, indicating the strongest inclination of Th2 immune responses (Fig. S11†).[59]

Rapid activation of immune response when encountering the re-invasion of pathogens is considered the crucial role of the vaccine. Therefore, the function to promote the proliferation and differentiation of immune cells is also essential for vaccines. ISA 206 is the most widely used commercial adjuvant of FMDV. This adjuvant can induce a high level of specific antibodies, but it cannot effectively promote the proliferation of T immune cells.[46,60] ISA 206 even has been reported to have an inhibitory effect on cellular immunity.[61] By comparing our T cell production results with those reported in the literature, it was found that our CD 8^+ T cell production results are generally consistent with the reported yields (ranges from 8–10%) by

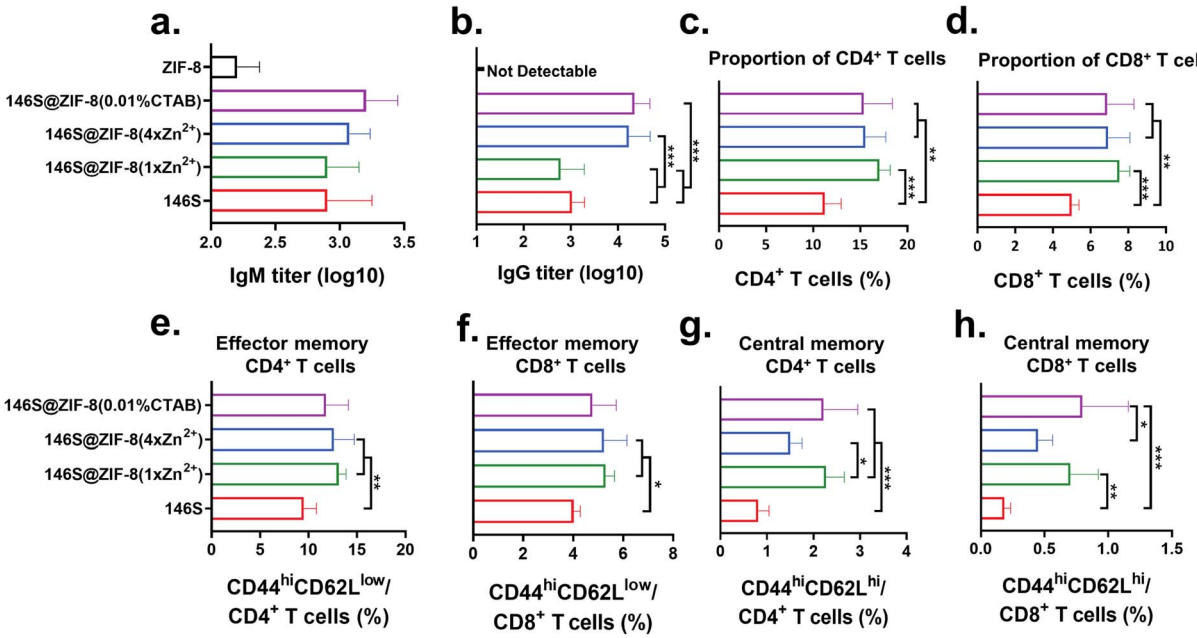

Fig. 6 Evaluation of the immune responses induced by subcutaneous injection of 146S@ZIF-8. (a) Specific IgM titers in the serum of mice 14 days post primary immunization and (b) IgG titers in the serum of mice 14 days post boosted immunization measured using ELISA ($n = 6$). The proportion of (c) $CD4^+$ T cells and (d) $CD8^+$ T cells in the splenocytes measured using flow cytometry ($n = 6$). Frequency of (e) effector memory $CD4^+$ T cells, (f) effector memory $CD8^+$ T cells, (g) central memory $CD4^+$ T cells, and (h) central memory $CD8^+$ T cells in the splenocytes in different formations measured using flow cytometry ($n = 6$). The asterisks indicate significant differences (*$P < 0.05$, **$P < 0.01$, and ***$P < 0.001$).

using naked FMDV and commercial ISA 206 formulation vaccine.[60,62,63] The absolute value of the $CD4^+$ T cell in our work was relatively lower than the results of other literature, which varies from 10% to 40%.[60–66] However, compared with naked 146S, both $CD4^+$ T and CD 8^+ T cells by using 146S@ZIF-8 were statistically higher (Fig. 6c and d).

Memory T cells, which include central memory T cells (T_{CM}, $CD44^{hi}CD62L^{hi}$) and effector memory T cells (T_{EM}, $CD44^{hi}CD62L^{low}$), are important components for memory immune responses, which have different functions. Generally, T_{EM} mediates the generation of protective memory by migrating to inflamed peripheral tissues and displaying immediate effector function when re-exposed to pathogens, whereas T_{CM} can provide reactive memory by homing to T cell areas of secondary lymphoid organs, and thus have little or no effector function, but readily proliferate and differentiate to effector cells in response to antigenic stimulation.[67] According to flow cytometry analysis (Fig. S12†), all three kinds of 146S@ZIF-8 generated more T_{EM} in both $CD4^+$ and $CD8^+$ T cells than the naked 146S did, but their promoting effects on T_{EM} were basically the same (Fig. 6e and f). For T_{CM}, the 146S@ZIF-8(1×Zn^{2+}) and 146S@ZIF-8(0.01% CTAB) groups are significantly more effective than the naked 146S, while the promoting effect of 146S@ZIF-8(4×Zn^{2+}) on T_{CM} was relatively weak (Fig. 6g and h), which may be due to its relatively higher cytotoxicity compared with the other two 146S@ZIF-8 groups (see below) and the inhibitory effect of a high concentration of Zn^{2+} on the function of T cells.[68]

Collectively, the immunization experiment results suggested that the 146S antigen could be effectively released from 146S@ZIF-8 *in vivo* to induce strong humoral and cellular immune responses in mice. More importantly, 146S@ZIF-8(4×Zn^{2+}) and 146S@ZIF-8(0.01% CTAB) even showed significantly improved immune responses, while in most of the reported studies, some immunopotentiators had to be included in the antigen@ZIF-8 system to obtain a satisfactory immune response. For instance, the antibody titer induced by TMV@ZIF-8 was just comparable to that by naked TMV.[22] Without adding Al^{3+} or/and CpG-ODN as adjuvants, OVA@ZIF-8 could only slightly increase the OVA-specific antibody.[14,69] By comparing the immune responses induced by the three 146S@ZIF-8, we can reasonably speculate that the appropriate particle size, morphology, and surface properties of ZIF-8, as well as the effective protection of the antigen from denaturation during the synthesis process, play crucial roles in the final immune effect of antigen@ZIF-8.

Biocompatibility and stability

The *in vitro* cytotoxicity of 146S@ZIF-8 was evaluated by Cell Counting Kit-8 (CCK-8) assay. 146S@ZIF-8(1×Zn^{2+}) basically showed no toxicity over a wide dose range from 20–200 μg mL^{-1}. The cells incubated with 146S@ZIF-8(4×Zn^{2+}) and ZIF-8 were severely inhibited at high ZIF-8 concentration, indicating dose-dependent toxicity. 146S@ZIF-8(0.01% CTAB) showed slight toxicity in the cells, but its cytotoxicity remained almost unchanged with the increased concentration. Even at 200 μg mL^{-1} of 146S@ZIF-8(0.01% CTAB), there was still about 80% cell viability, which will enable its safe application over a wide dose range (Fig. 7a). According to the approximate weight ratio of 146S in the synthesized 146S@ZIF-8 measured by TGA analysis (Fig. 4c) and the immune dose of the antigen, the concentration of immunized 146S@ZIF-8(1×Zn^{2+}), 146S@ZIF-8(4×Zn^{2+}), and 146S@ZIF-8(0.01% CTAB) in the blood (*ca.* 1

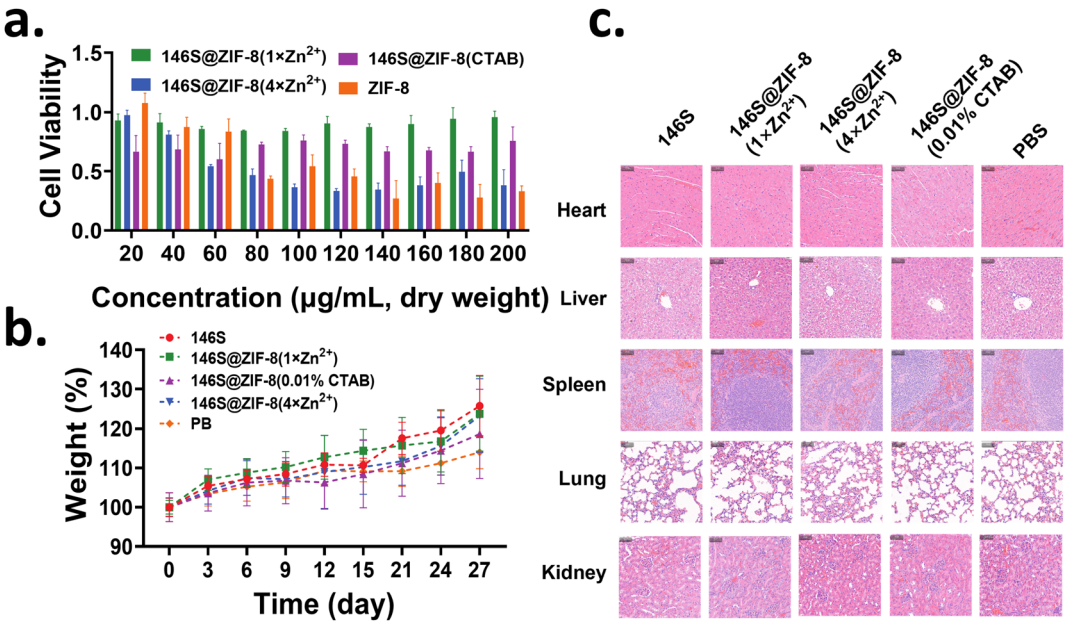

Fig. 7 Safety evaluation of 146S@ZIF-8. (a) The cytotoxic effect of 146S@ZIF-8; (b) body weight of mice in each group within 28 days after immunization ($n = 6$); (c) representative H&E-stained tissues of the mice on day 3 post subcutaneous immunization. Scale bar: 50 μm.

mL) was estimated to be about 10, 30, and 20 μg mL^{-1}, respectively, which were far lower than the dose causing a severe toxic reaction with cells.

Then, the *in vivo* biocompatibility of 146S@ZIF-8 was evaluated in a mice model. The mice subcutaneously immunized with all three kinds of 146S@ZIF-8 showed similar body weight growth curves compared with the mice immunized with the naked antigen and PBS (Fig. 7b). No physiological symptoms were observed in each group. The hematoxylin and eosin (H&E) staining of the main organs of mice collected on day 3 after subcutaneous immunization, including the heart, liver, spleen, lung, and kidney, showed no damage in each group (Fig. 7c). In order to evaluate the acute toxicity of the drug *in vivo*, the blood biochemical indicators of mice were evaluated three days after immunization. The results showed that there was no significant difference in biochemical parameters related to liver and kidney function after immunization (Fig. S13†), and no abnormal physiological indicators caused by drug immunization were found.

The stability of ZIF-8 under physiological conditions is critical for its biomedical application. The phosphate buffer (PBS) is known to decompose ZIF-8 by releasing Zn^{2+} to form insoluble amorphous zinc phosphates.[70,71] According to SEM images presented in Fig. S14,† there was no obvious change in the morphologies of the three 146S@ZIF-8 materials in PBS at 4 °C. However, when incubated in PBS at 37 °C, flower-like structures (zinc phosphates) were formed in 146S@ZIF-8(4×Zn^{2+}) and 146S@ZIF-8(0.01% CTAB) at 24 h, while the morphology of 146S@ZIF-8(1×Zn^{2+}) remained unchanged. We speculated that the differences in the stability of the three ZIF-8 materials were mainly due to their differences in their size and dispersity. 146S@ZIF-8(1×Zn^{2+}) formed aggregations, and thus will slow the chelation of Zn^{2+} by PO_4^{3-}. In contrast, 146S@ZIF-8(0.01% CTAB) with the smallest size and thinnest ZIF-8 layer was more susceptible to decomposition. The rapid decomposition of 146S@ZIF-8(4×Zn^{2+}) and 146S@ZIF-8(0.01% CTAB) may be beneficial to releasing antigens and inducing immune response in animals, as demonstrated by high IgG levels (Fig. 6b).

Conclusions

In this study, we reported for the first time the successful synthesis of crystalline ZIF-8 on 146S, which is extremely sensitive to pH and temperature. Our results showed that lowering the pH of the 2-MIM solution to 9.0 is an effective strategy to balance the 146S stability and the ZIF-8 crystal growth. The morphology and size of 146S@ZIF-8 can be further optimized by increasing the amount of Zn^{2+} used or by adding CTAB. Under optimal conditions, 146S@ZIF-8(0.01% CTAB) with a uniform size of about 49 nm was synthesized, and was speculated to be composed of single-146S particles armored with nanometer-scale ZIF-8 crystal networks. DSF analysis demonstrated that the structural integrity of 146S was well preserved, and its thermal stability was significantly increased by as high as about 5 °C after ZIF-8 encapsulation. More importantly, the well-controlled size and morphology enabled more efficient cell uptake and lysosomal escape of 146S@ZIF-8(0.01% CTAB). As a consequence, compared with naked 146S, the immunization of 146S@ZIF-8(4×Zn^{2+}) and 146S@ZIF-8(0.01% CTAB) induced about 10-times higher antibody titer and significantly higher cellular immunogenicity response in mice, without the need for co-delivery of any other immunopotentiator as used in most of the reported studies.[14,22,69] This result suggested that adjusting 146S@ZIF-8 to a nano-size with appropriate surface properties is effective and crucial to exert the adjuvant effects of ZIF-8. Though the applicability of this mineralization strategy in other antigens and the detailed mechanisms of *in vivo* antigen release from 146S@ZIF-8 need to be further studied, the successful synthesis of 146S@ZIF-8 with a desired morphology, excellent biocompatibility, significantly improved thermostability and enhanced immunogenicity demonstrated by the present work provides an effective biomimetic mineralization strategy on the environment-sensitive antigens, and thus expanded the application of MOFs in vaccine delivery.

Experimental

Materials

2-methylimidazole (98%) was purchased from Energy Chemical Co., Ltd (Shanghai, China). $ZnCl_2$ was purchased from Macklin Biochemical Co., Ltd (Shanghai, China). Cetyltrimethylammonium bromide (CTAB) was purchased from Aladdin Biochemical Technology Co., Ltd (Shanghai, China). Sodium ethylene diamine tetraacetic acid (EDTA-Na_2) was purchased from Sinopharm Chemical Reagent Co., Ltd (Shanghai, China). Nucleic acid dye SYBR GREEN II, 4% tissue fix solution, and DAPI dye were purchased from Beijing Solarbio Science & Technology Co., Ltd. (Beijing, China). The Formvar support film was purchased from Zhongjingkeyi Film Technology Co., Ltd. (Beijing, China). The cell Counting Kit-8 (CCK-8) kit was purchased from LABLEAD. Inc (Beijing, China). 3′,6′-Dihydroxy-5-isothiocyanato-3H-spiro[isobenzofuran-1,9′-xanthen]-3-one (FITC), PRIM-1640, 0.25% trypsin–EDTA (1×), PBS (1×), penicillin–streptomycin solution and LysoTracker™ Red DND-99 lysosomal probe were purchased from Thermo Fisher Scientific (Massachusetts, USA). Dendritic cells 2.4 were saved by our laboratory. All other reagents were all analytical grade and used without further treatment. Unless otherwise specified, deionized water for injection was used for solution preparation.

Purification of FMDV 146S

Inactivated O strain 146S (Lanzhou Veterinary Research Institute, Lanzhou, China) was purified under well-established conditions as reported previously.[72] The purified 146S was formulated in phosphate buffer (PB, 20 mM pH 8.0) containing 0.15 M $(NH_4)_2SO_4$. Unless otherwise specifically stated, this buffer solution, named protein stabilization buffer (PSB), was used as a basic buffer in the subsequent experimental steps. The purity and the contents of 146S were measured by high-performance size-exclusion chromatography (HPSEC).[30]

Stability of 146S in the 2-MIM solution of different pHs

2-MIM solutions (0.64 M) of different pHs were prepared in deionized water by adjusting the pH with 2 M HCl. 200 μg mL^{-1} 146S in PSB was mixed with the 2-MIM solutions at a volumetric ratio of 1 : 5.5. The remaining content of intact 146S in the mixture solution was quantitatively determined by HPSEC immediately after mixing.

Preparation of ZIF-8 and 146S@ZIF-8

ZIF-8 was prepared according to a reported method[34] with slight modification. Briefly, 6 mL of 0.64 M 2-MIM solution with pHs ranging from 10.9 (un-adjusted) to 8.5 (adjusted with 2 M HCl) was mixed with 1.5 mL PSB; then 0.75 mL of 83 mM $ZnCl_2$ solution was added under magnetic stirring. After 48 hours of magnetic stirring at 26 °C, the ZIF-8 synthesized was collected from the reactant mixture by centrifugation at 10 000 rpm for 10 min. The white precipitate was collected and washed twice with PSB and re-suspend in 1.5 mL of the same buffer for further characterization.

146S@ZIF-8 was prepared following the same steps described above, by mixing 1.5 mL of 200 μg mL^{-1} 146S with 6 mL of 0.64 M 2-MIM solution with pH pre-adjusted to 9.0, followed by adding 0.75 mL of 83 mM $ZnCl_2$ solution. During preparation, a 150 μL sample was withdrawn at different time intervals and centrifuged. The remaining 146S in the supernatant was detected by HPSEC, SDS-PAGE, and agarose gel electrophoresis (AGE). The reaction was terminated when the remaining content of 146S in the supernatant was less than 10% of its initial content as measured by HPSEC. The precipitation was collected and washed twice with PSB and re-suspend in 1.5 mL of the same buffer for further characterization.

To optimize the morphology and size of 146S@ZIF-8, the amount of $ZnCl_2$ solution used for synthesis was increased to 2, 3, and 4 times without changing the amounts of other reagents. The prepared substance was named 146S@ZIF-8($2\times Zn^{2+}$), 146S@ZIF-8($3\times Zn^{2+}$), and 146S@ZIF-8($4\times Zn^{2+}$) in the following context. In another attempt, CTAB using as a capping agent was included in the 2-MIM solution to make the final CTAB concentrations in the reaction system of 0.0025% (w/v), 0.01% (w/v), 0.025% (w/v), respectively. The prepared substances were named 146S@ZIF-8(0.0025% CTAB), 146S@ZIF-8(0.01% CTAB) and 146S@ZIF-8(0.025% CTAB), respectively.

Characterization of ZIF-8 and 146S@ZIF-8

The morphology and surface properties of ZIF-8 and 146S@ZIF-8 were observed by scanning electron microscopy (SEM, JSM-7800, JEOL, Japan) with energy dispersive spectroscopy (EDS, Oxford Instruments, UK) and transmission electron microscopy (TEM, JEM-1400, JEOL, Japan). The Fourier transform infrared spectroscopy (FT-IR) absorption curve was recorded by using an iS50 FT-IR (Thermo Fisher Scientific, USA). The PXRD pattern of 146S@ZIF-8 was collected at ambient temperature on a SmartLab 9 kW (Rigaku Corporation, Japan) with a step size of 0.01° in 2θ, and a 2θ range of 5° to 50°. The particle size and surface ζ-potential of 146S@ZIF-8 were recorded by Dynamic Light Scattering (Malvern, UK). The composition of 146S@ZIF-8 was determined by thermogravimetric analysis (TGA) by using an SDT Q600 (TA instruments, USA).

Quantification of 146S

The purity and the contents of solution-based 146S were measured by HPSEC.[30] The content of 146S in ZIF-8 was quantified by SDS-PAGE by scanning the electrophoretic gel using an Amersham Typhoon (GE Healthcare, USA). By comparing the gray-scale of the sample with the calibration curve prepared with 146S of known concentration, the 146S concentration in ZIF-8 was calculated using ImageQuanTL software (GE Healthcare, USA).

Thermostability of 146S@ZIF-8

The thermostability of 146S in solution and encapsulated in ZIF-8 was measured by differential scanning fluorescence (DSF) analysis according to our published method.[41] Briefly, 18 μL solution containing 146S was mixed with 2 μL 1 : 100-fold diluted SYBR Green II (Solarbio, China). The experiments were performed using a real-time PCR instrument (Applied Biosystem, USA) at a scan rate of 1 °C min^{-1} from 25 °C to 95 °C. The T_m value corresponding to the dissociation of 146S to 12S was calculated according to the maximum of the first derivative [d(RFU)/dT] plot of the fluorescence curve.

Release behavior of 146S from 146S@ZIF-8

To verify the encapsulation of 146S and investigate its release behavior from 146S@ZIF-8, 1 M EDTA solution was added to the 146S@ZIF-8 suspension at a volumetric ratio of 1 : 10. After 24 hours' incubation on a rotating mixer at 4 °C, the mixture solution was centrifuged, and then the supernatant and precipitate were analyzed by SDS-PAGE, HPSEC (for the supernatant sample only), SEM, TEM, and DSF.

Uptake of 146S@ZIF-8 by DC 2.4

146S was mixed with an overdose of FITC fluorescence dye and stored at 4 °C for 12 hours. The unlabeled FITC was removed by using a 30 kDa ultrafiltration tube (Millipore, USA), and the final FITC-labeled 146S was concentrated to 200 μg mL^{-1} and then used for FITC-146S@ZIF-8 preparation. To evaluate the transmembrane transport efficiency of 146S@ZIF-8, DC 2.4 cells were seeded in a 24-well cell culture plate (Corning, USA), and FITC-146S@ZIF-8 with an equivalent 146S dose of 4 μg was added to the culture medium. After 4 hours of incubation, the cells were digested with trypsin and washed with cell staining buffer (Biolegend, USA), and the $FITC^+$ cells were analyzed with a flow cytometer (BD, USA). The uptake of solution-based 146S by DC 2.4 was also determined for comparison.

Lysosomal escape

To evaluate the co-localization and escape ability with the lysosome of 146S@ZIF-8, DC 2.4 cells were seeded in confocal dishes (Biosharp, China) and pre-incubated for 24 hours. Next, the culture medium was replaced by the medium with 4 μg

FITC-146S@ZIF-8 for another 0.5, 1, 2, 4, 6, and 8 hours. The cells were then stained with LysoTracker Red and DAPI to visualize the lysosomes and nucleus using a confocal laser scanning microscope (CLSM, Leica, Germany).

Immunization

Female Balb/c mice (aged 6–8 weeks) were purchased from Beijing SiPeiFu Biotechnology Co., Ltd. (Beijing, China). The mice were divided into five groups randomly, with six mice in each group. The naked 146S group, 146S@ZIF-8($1\times Zn^{2+}$) group, 146S@ZIF-8($4\times Zn^{2+}$) group, 146S@ZIF-8(0.01% CTAB) group, and ZIF-8 (without antigens) were all immunized subcutaneously with various samples at 100 μL (containing 4 μg 146S). The PBS group was only immunized subcutaneously with 100 μL PBS buffer as a control. All mice were immunized on day 0 and boosted immunized on day 14. To maintain the consistency of the doses of the antigen in each group, all formulations were freshly made before immunization. Serum from orbital blood was collected on days 14 and 28 post primary immunization.

Protocols for animal experiments were performed in strict accordance with the Experimental Animal Guidelines for Ethical Review of Animal Welfare (GB/T 35-892-2018) and were approved by the Committee on the Ethics of Animal Experiments of the Institute of Process Engineering at the Chinese Academy of Sciences (Beijing, China).

Determination of specific antibody titers

The levels of 146S-specific antibody titers, including serum IgG, IgG1, and IgG2a of the immunized mice, were assayed by enzyme-linked immunosorbent assay (ELISA). Briefly, 96-well half-area ELISA plates (Costar, USA) were coated with 5 μg 146S per well and subsequently blocked with blocking buffer (BioLegend, USA). The serum was serially diluted twofold with the blocking buffer. After incubation at 37 °C for 1 hour, HRP-conjugated anti-mouse antibodies (IgM, IgG, IgG1 and IgG2a) were then added to each well at a 1 : 5000 dilution and incubated at room temperature for 1 hour. After washing with PBST, 3,3′,5,5′-tetramethylbenzidine (TMB) solution (Thermo, USA) was added to each plate in the dark for 15 min. Finally, the reactions were stopped by adding 2 M H_2SO_4. The optical density (OD) was read at 450 nm by using a microplate reader (Thermo, USA). The end-point titers were determined by the maximal serum dilution that exceeded twice the OD values of the control wells.

Stability of 146S@ZIF-8 in PBS

Three kinds of 146S@ZIF-8 (containing 40 μg mL^{-1} 146S) were resuspended with PBS and incubated at 4 or 37 °C for 6, 12, and 24 h. The suspensions were centrifuged and precipitates were collected, washed three times and resuspended with deionized water. Changes in the morphology were observed by SEM.

Activation of immune cells in splenocytes

28 days after the primary immunization, the mice were euthanized. The spleen was obtained by dissection, ground on a 40 μm cell mesh (Biologix, USA), lysed red blood cells, and prepared into a single cell suspension, which was then stimulated by 4 μg 146S, and placed in a cell incubator (37 °C, 5% CO_2) for 40 hours. The cell suspension was centrifuged to remove the medium, and the cells were washed with cell staining buffer (Biolegend, USA). The antibodies, including FITC anti CD4, BV510 anti-CD8, PE anti CD44, and BV605 anti-CD62L (Biolegend, USA) pre-diluted to the working concentration with cell staining buffer, were added to stain the cells. After staining for 30 min at 4 °C, the cells were washed again to remove unbound antibodies, and differentiated by FACS Celesta™ Flow Cytometry (BD, USA).

Biocompatibility evaluation

The cellular cytotoxicity of 146S@ZIF-8 was evaluated using a Cell Counting Kit-8 (CCK-8) colorimetric assay method. Briefly, DC 2.4 cells were inoculated and pre-cultured in the cell culture plate for 24 hours, and then incubated with different amounts of 146S@ZIF-8 for 4 hours. Then the CCK-8 reagent was added followed by another 3 hours of incubation. The absorption at 450 nm wavelength was recorded by using a microplate reader, and the absorption at 650 nm wavelength was used as the reference.

To evaluate the *in vivo* toxicity of 146S@ZIF-8, female Balb/c mice were subcutaneously immunized with the naked 146S antigen or 146S@ZIF-8 at the immunization dose. Serum was collected 3 days after immunization, and the biochemical parameters, including alanine aminotransferase, aspartate aminotransferase, alkaline phosphatase, albumin (ALB), γ-glutamyltransferase (GGT), direct bilirubin (DBIL), bilirubin total (TBIL), total bile acid (TBA), creatine (CR), and uric acid (UA), were determined by using a Chemray 240 automatic biochemical analyzer (Rayto, China). The main organs of mice, including the heart, liver, spleen, lung, and kidney, were collected for hematoxylin and eosin (H&E) staining analysis.

Statistical analysis

Data analysis was performed with Origin 7.0 and GraphPad Prism 7.0 software and presented as the mean with standard deviation (SD). The statistical significance of differences was determined by one-way ANOVA. P values of less than 0.05 were considered statistically significant. Asterisks indicate significant differences ($^*P < 0.05$, $^{**}P < 0.01$, and $^{***}P < 0.001$).

Author contributions

L. W. and X. L. contributed equally. L. W.: conceptualization, investigation, methodology, and writing-original draft. X. L.: conceptualization, investigation, methodology, and supervision. Y. S.: investigation and methodology. H. Z.: investigation and methodology. Z. L.: validation. Z. S.: supervision. R. Y.: supervision. S. Z.: conceptualization, formal analysis, funding acquisition, supervision, and writing-review & editing.

Conflicts of interest

The authors declare no competing financial interest.

Acknowledgements

Financial support from the National Natural Science Foundation of China (No. 31970872 and 21821005) is acknowledged.

References

1 G. Lu, S. Z. Li, Z. Guo, O. K. Farha, B. G. Hauser, X. Y. Qi, Y. Wang, X. Wang, S. Y. Han, X. G. Liu, J. S. DuChene, H. Zhang, Q. C. Zhang, X. D. Chen, J. Ma, S. C. J. Loo, W. D. Wei, Y. H. Yang, J. T. Hupp and F. W. Huo, *Nat. Chem.*, 2012, **4**, 310–316.
2 I. Tibbetts and G. E. Kostakis, *Molecules*, 2020, **25**, 1291.
3 S. M. Feng, X. L. Zhang, D. Y. Shi and Z. Wang, *Front. Chem. Sci. Eng.*, 2021, **15**, 221–237.
4 J. W. M. Osterrieth and D. Fairen-Jimenez, *Biotechnol. J.*, 2021, **16**, 2000005.
5 P. Horcajada, R. Gref, T. Baati, P. K. Allan, G. Maurin, P. Couvreur, G. Ferey, R. E. Morris and C. Serre, *Chem. Rev.*, 2012, **112**, 1232–1268.
6 L. Zhang, Z. Wang, Y. Zhang, F. Cao, K. Dong, J. Ren and X. Qu, *ACS Nano*, 2018, **12**, 10201–10211.
7 Y. F. Feng, H. R. Wang, S. N. Zhang, Y. Zhao, J. Gao, Y. Y. Zheng, P. Zhao, Z. J. Zhang, M. J. Zaworotko, P. Cheng, S. Q. Ma and Y. Chen, *Adv. Mater.*, 2019, **31**, 7.
8 W.-H. Chen, G.-F. Luo, M. Vázquez-González, R. Cazelles, Y. S. Sohn, R. Nechushtai, Y. Mandel and I. Willner, *ACS Nano*, 2018, **12**, 7538–7545.
9 H. Ranji-Burachaloo, A. Reyhani, P. A. Gurr, D. E. Dunstan and G. G. Qiao, *Nanoscale*, 2019, **11**, 5705–5716.
10 Z. Teng, F. Hou, M. Bai, J. Li, J. Wang, J. Wu, J. Ru, M. Ren, S. Sun and H. Guo, *J. Mater. Chem. B*, 2022, **10**, 2853–2864.
11 R. Singh, J. F. White, M. de Vries, G. Beddome, M. Dai, A. G. Bean, X. Mulet, D. Layton and C. M. Doherty, *Acta Biomater.*, 2022, **142**, 320–331.
12 P. Hao, X. Wu, L. Wang, S. Wei, H. Xu, W. Huang, Y. Li, T. Zhang and X. Zan, *Bioconjugate Chem.*, 2020, **31**, 1917–1927.
13 S. B. Li, M. Dharmarwardana, R. P. Welch, Y. X. Ren, C. M. Thompson, R. A. Smaldone and J. J. Gassensmith, *Angew. Chem., Int. Ed.*, 2016, **55**, 10691–10696.
14 X. Zhong, Y. Zhang, L. Tan, T. Zheng, Y. Hou, X. Hong, G. Du, X. Chen, Y. Zhang and X. Sun, *J. Controlled Release*, 2019, **300**, 81–92.
15 Y. Zhang, F. M. Wang, E. G. Ju, Z. Liu, Z. W. Chen, J. S. Ren and X. G. Qu, *Adv. Funct. Mater.*, 2016, **26**, 6454–6461.
16 O. R. Brohlin, R. N. Ehrman, F. C. Herbert, Y. H. Wijesundara, A. Raja, A. Shahrivarkevishahi, S. D. Diwakara, R. A. Smaldone and J. J. Gassensmith, *ACS Appl. Nano Mater.*, 2022, **5**, 13697–13704.
17 H. E. Moses, C. A. Brandly and E. E. Jones, *Science*, 1947, **105**, 477–479.
18 S. F. Ausar, J. Rexroad, V. G. Frolov, J. L. Look, N. Konar and C. R. Middaugh, *Mol. Pharm.*, 2005, **2**, 491–499.
19 X. Lin, Y. L. Yang, Y. M. Song, S. Li, X. Zhang, Z. G. Su and S. P. Zhang, *J. Virol.*, 2021, **95**, e02431–e02420.
20 M. F. Bachmann and G. T. Jennings, *Nat. Rev. Immunol.*, 2010, **10**, 787–796.
21 M. Sindoro and S. Granick, *J. Am. Chem. Soc.*, 2014, **136**, 13471–13473.
22 M. A. Luzuriaga, R. P. Welch, M. Dharmarwardana, C. E. Benjamin, S. Li, A. Shahrivarkevishahi, S. Popal, L. H. Tuong, C. T. Creswell and J. J. Gassensmith, *ACS Appl. Mater. Interfaces*, 2019, **11**, 9740–9746.
23 R. Riccò, W. Liang, S. Li, J. J. Gassensmith, F. Caruso, C. Doonan and P. Falcaro, *ACS Nano*, 2018, **12**, 13–23.
24 Y. Zhang, H. Hao, J. Lin, Z. Ma, H. Li, Z. Nie, Y. Cui, Z. Guo, Y. Zhang, X. Wang and R. Tang, *ACS Appl. Mater. Interfaces*, 2022, **14**, 39873–39884.
25 A. Kotecha, J. Seago, K. Scott, A. Burman, S. Loureiro, J. S. Ren, C. Porta, H. M. Ginn, T. Jackson, E. Perez-Martin, C. A. Siebert, G. Paul, J. T. Huiskonen, I. M. Jones, R. M. Esnouf, E. E. Fry, F. F. Maree, B. Charleston and D. I. Stuart, *Nat. Struct. Mol. Biol.*, 2015, **22**, 788–794.
26 S. C. Han, H. C. Guo and S. Q. Sun, *Arch. Virol.*, 2015, **160**, 1–16.
27 Y. L. Yang, Q. Z. Zhao, Z. J. Li, L. J. Sun, G. H. Ma, S. P. Zhang and Z. G. Su, *Vaccine*, 2017, **35**, 2413–2419.
28 F. F. Maree, B. Blignaut, T. A. P. de Beer and E. Rieder, *PLoS One*, 2013, **8**, 462–472.
29 H. W. van Vlijmen, S. Curry, M. Schaefer and M. Karplus, *J. Mol. Biol.*, 1998, **275**, 295–308.
30 Y. L. Yang, H. Li, Z. J. Li, Y. Zhang, S. P. Zhang, Y. Chen, M. R. Yu, G. H. Ma and Z. G. Su, *Vaccine*, 2015, **33**, 1143–1150.
31 H. Feng, Z. Y. Li, W. J. Xie, Q. B. Wan, Y. W. Guo, J. Y. Chen, J. Wang and X. B. Pei, *Chem. Eng. J.*, 2022, **430**, 11.
32 J. J. Beh, J. K. Lim, E. P. Ng and B. S. Ooi, *Mater. Chem. Phys.*, 2018, **216**, 393–401.
33 S. R. Venna, J. B. Jasinski and M. A. Carreon, *J. Am. Chem. Soc.*, 2010, **132**, 18030–18033.
34 K. Kida, M. Okita, K. Fujita, S. Tanaka and Y. Miyake, *CrystEngComm*, 2013, **15**, 1794–1801.
35 Y. Pan, Y. Liu, G. Zeng, L. Zhao and Z. Lai, *Chem. Commun.*, 2011, **47**, 2071–2073.
36 W.-H. Chen, M. Vázquez-González, A. Zoabi, R. Abu-Reziq and I. Willner, *Nat. Catal.*, 2018, **1**, 689–695.
37 A. F. Ogata, A. M. Rakowski, B. P. Carpenter, D. A. Fishman, J. G. Merham, P. J. Hurst and J. P. Patterson, *J. Am. Chem. Soc.*, 2020, **142**, 1433–1442.
38 J. Cravillon, R. Nayuk, S. Springer, A. Feldhoff, K. Huber and M. Wiebcke, *Chem. Mater.*, 2011, **23**, 2130–2141.
39 W. Morris, C. J. Stevens, R. E. Taylor, C. Dybowski, O. M. Yaghi and M. A. Garcia-Garibay, *J. Phys. Chem. C*, 2012, **116**, 13307–13312.
40 S. Li and J. J. Gassensmith, *Protein Scaffolds*, 2018, **1798**, 95–108.
41 Y. M. Song, Y. L. Yang, X. Lin, X. N. Li, X. Zhang, G. H. Ma, Z. G. Su and S. P. Zhang, *Vaccine*, 2020, **38**, 2904–2912.

42 F. H. Niesen, H. Berglund and M. Vedadi, *Nat. Protoc.*, 2007, **2**, 2212–2221.
43 J. Zhao, H. Li, Y. Han, R. Li, X. Ding, X. Feng and B. Wang, *J. Mater. Chem. A*, 2015, **3**, 12145–12148.
44 S. S. Bhatnagar and D. I. Shrivastava, *Nature*, 1941, **147**, 58.
45 Y. Pan, D. Heryadi, F. Zhou, L. Zhao, G. Lestari, H. Su and Z. Lai, *CrystEngComm*, 2011, **13**, 6937–6940.
46 Y. Q. Wang, Y. Liu, Y. X. Wang, Y. J. Wu, P. Y. Jia, J. J. Shan, J. Wu, G. H. Ma and Z. G. Su, *Int. Immunopharmacol.*, 2016, **39**, 84–91.
47 F. J. Lyu, Y. F. Zhang, R. N. Zare, J. Ge and Z. Liu, *Nano Lett.*, 2014, **14**, 5761–5765.
48 Y. Zhang, F. Wang, E. Ju, Z. Liu, Z. Chen, J. Ren and X. Qu, *Adv. Funct. Mater.*, 2016, **26**, 6454–6461.
49 H. Zhang, W. Chen, K. Gong and J. Chen, *ACS Appl. Mater. Interfaces*, 2017, **9**, 31519–31525.
50 V. Holzapfel, A. Musyanovych, K. Landfester, M. R. Lorenz and V. Mailander, *Mater. Chem. Phys.*, 2005, **206**, 2440–2449.
51 N. E. Eleraky, N. K. Swarnakar, D. F. Mohamed, M. A. Attia and G. M. Pauletti, *AAPS PharmSciTech*, 2020, **21**, 88.
52 Z. Zhou, A. Badkas, M. Stevenson, J.-Y. Lee and Y.-K. Leung, *Int. J. Pharm.*, 2015, **487**, 81–90.
53 O. P. Joffre, E. Segura, A. Savina and S. Amigorena, *Nat. Rev. Immunol.*, 2012, **12**, 557–569.
54 N. Juleff, M. Windsor, E. A. Lefevre, S. Gubbins, P. Hamblin, E. Reid, K. McLaughlin, P. C. L. Beverley, I. W. Morrison and B. Charleston, *J. Virol.*, 2009, **83**, 3626–3636.
55 P. V. Barnett, S. J. Cox, N. Aggarwal, H. Gerber and K. C. McCullough, *Vaccine*, 2002, **20**, 3197–3208.
56 J. Pega, D. Bucafusco, S. D. Giacomo, J. M. Schammas, D. Malacari, A. V. Capozzo, J. Arzt, C. Pérez-Beascoechea, E. Maradei, L. L. Rodríguez, M. V. Borca and M. Pérez-Filgueira, *J. Virol.*, 2013, **87**, 2489–2495.
57 M. G. Rao, G. Butchaiah and A. K. Sen, *Vet. Microbiol.*, 1994, **39**, 135–143.
58 J. C. Cox and A. R. Coulter, *Vaccine*, 1997, **15**, 248–256.
59 S. Li, Y. L. Yang, X. Lin, Z. J. Li, G. H. Ma, Z. G. Su and S. P. Zhang, *Vaccine*, 2020, **38**, 2478–2486.
60 F. Hou, Z. Teng, J. Ru, H. Liu, J. Li, Y. Zhang, S. Sun and H. Guo, *Nanomedicine*, 2022, **42**, 102541.
61 S. Li, Y. Yang, X. Lin, Z. Li, G. Ma, Z. Su and S. Zhang, *Mol. Pharm.*, 2020, **17**, 2952–2963.
62 D. Wang, H. Cao, J. Li, B. Zhao, Y. Wang, A. Zhang and J. Huang, *Res. Vet. Sci.*, 2019, **124**, 191–199.
63 Q. Li, X. Ba, H. Cao, X. Weng, Y. Yang, B. Wang and A. Zhang, *J. Funct. Foods*, 2021, **87**, 104800.
64 W. Yin, D. Xuan, H. Wang, M. Zhou, B. Deng, F. Ma, Y. Lu and J. Zhang, *ACS Appl. Bio Mater.*, 2022, **5**, 3095–3106.
65 C.-X. Zhou, D. Li, Y.-L. Chen, Z.-J. Lu, P. Sun, Y.-M. Cao, H.-F. Bao, Y.-F. Fu, P.-H. Li, X.-W. Bai, B.-X. Xie and Z.-X. Liu, *BMC Vet. Res.*, 2014, **10**, 2.
66 H. Liu, Z. Teng, H. Dong, J. Li, S. Waheed Abdullah, Y. Zhang, J. Wu, H. Guo and S. Sun, *Virology*, 2023, **579**, 94–100.
67 F. Sallusto, J. Geginat and A. Lanzavecchia, *Annu. Rev. Immunol.*, 2004, **22**, 745–763.
68 R. K. Chandra, *JAMA, J. Am. Med. Assoc.*, 1984, **252**, 1443–1446.
69 G. Zhang, X. Fu, H. Sun, P. Zhang, S. Zhai, J. Hao, J. Cui and M. Hu, *ACS Appl. Mater. Interfaces*, 2021, **13**, 13978–13989.
70 M. Taheri, D. Ashok, T. Sen, T. G. Enge, N. K. Verma, A. Tricoli, A. Lowe, D. R. Nisbet and T. Tsuzuki, *Chem. Eng. J.*, 2021, **413**, 127511.
71 M. d. J. Velásquez-Hernández, R. Ricco, F. Carraro, F. T. Limpoco, M. Linares-Moreau, E. Leitner, H. Wiltsche, J. Rattenberger, H. Schröttner, P. Frühwirt, E. M. Stadler, G. Gescheidt, H. Amenitsch, C. J. Doonan and P. Falcaro, *CrystEngComm*, 2019, **21**, 4538–4544.
72 H. Li, Y. L. Yang, Y. Zhang, S. P. Zhang, Q. Zhao, Y. Y. Zhu, X. Q. Zou, M. R. Yu, G. H. Ma and Z. G. Su, *Protein Expression Purif.*, 2015, **113**, 23–29.